Inorganic Chemistry

pubs.acs.org/IC Article

Bis(CBT)palladium(II) Derivatives (CBT = *m*-carborane-1-thiolate): Synthesis, Molecular Structure, and Physicochemical Properties of *cis*-[(bipy)Pd(CBT)$_2$] and *trans*-[(py)$_2$Pd(CBT)$_2$]

Noemi Bellucci, Maria Pia Donzello,* Mario Amati,* Elisa Viola, Corrado Rizzoli,* Claudio Ercolani, Giampaolo Ricciardi, and Angela Rosa

Cite This: https://doi.org/10.1021/acs.inorgchem.1c01092 Read Online

ABSTRACT: The new synthesized Pd^{II} complex *cis*-[(bipy)Pd(CBT)$_2$] (bipy = 2,2′-bipyridyl; CBT = *m*-carborane-1-thiolate anion), which is a potential BNCT (boron neutron capture therapy) agent and of structure elucidated by single-crystal X-ray work, has been studied by infrared (IR) and ultraviolet−visible light (UV−vis) spectra and its properties compared with those of the previously reported and also the structurally characterized analogue *trans*-[(py)$_2$Pd(CBT)$_2$]. This *trans* species, prepared via a direct method, was previously isolated from a pyridine solution, consequent to the occurring releasing of the external Pd(CBT)$_2$ moieties of the porphyrazine macrocycle [{Pd(CBT)$_2$}$_4$LZn]·*x*H$_2$O (L = tetrakis-2,3-[5,6-di(2-pyridyl)pyrazino]-porphyrazinato anion), which is an active photosensitizer in photodynamic therapy (PDT) and a potential bimodal PDT/BNCT agent. The UV-vis spectral behavior of both *cis* and *trans* species in CHCl$_3$ solution and in the gas phase has been examined in detail by density functional theory (DFT) and time-dependent density functional theory (TDDFT) studies devoted to explain their distinct behavior observed in the region of 400−500 nm, as determined by the presence in the *cis* structure of a vicinal arrangement of the two CBT groups, an ensemble of results closely similar to those observed for the macrocycles [{Pd(CBT)$_2$}$_4$LM]·*x*H$_2$O (M = Mg^{II}(H$_2$O), Zn^{II}, Pd^{II}). It has also been experimentally proved the tendency of the *cis* isomer in CHCl$_3$/pyridine solution to be changed to the respective *trans* analogue, with conversion occurring in two steps, as interpreted by detailed DFT studies.

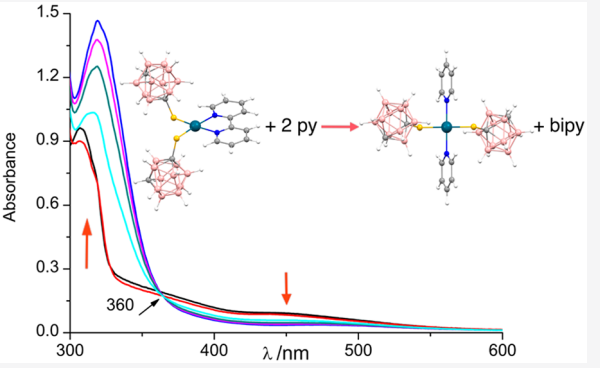

INTRODUCTION

Boron neutron capture therapy (BNCT) clinical trials in brain tumor patients started about 50 years ago and two low-molecular-weight clinically passed BNCT agents are presently used, i.e., sodium mercaptoundecahydro-closo-dodecaborate Na$_2$B$_{12}$H$_{11}$SH (BSH) and borylphenylalanine (BPA).[1] Advances in synthetic chemistry have led to significant progress in the development of tumor targeting boron delivery agents, such as the boron-containing isomeric carboranes, displaying a high potential as BNCT agents, because of their unique properties.[2] Among the so-called third-generation boron delivery agents, boronated porphyrins appear to be highly promising BNCT agents, because they can combine their potentialities in photodinamic therapy (PDT) in connection with BNCT.[3] Recent work allowed some of us to report on the neutral pentanuclear pyrazinoporphyrazine complexes of formula [{Pd(CBT)$_2$}$_4$LM·*x*H$_2$O (L = tetrakis-2,3-[5,6-di(2-pyridyl)pyrazino]porphyrazinato anion; M = Mg^{II}(H$_2$O), Zn^{II}, Pd^{II}) carrying peripheral *m*-carborane-1-thiolate groups (CBT) (Figure 1A),[4] and on the parent porphyrazine species [{Pd(CBT)$_2$}$_4$Py$_8$PzM]·*x*H$_2$O (Py$_8$Pz = octakis(2-pyridyl)-porphyrazinato anion; M = Mg^{II}(H$_2$O), Zn^{II}).[5] These two series of pentanuclear species behave as active photosensitizers in PDT and perspectives are also open for their use, because of their high boron content, in the area of BNCT. In ref 4, it has also been reported formation of the species *trans*-[(py)$_2$Pd(CBT)$_2$], appearing as an interesting potential BNCT agent of low molecular weight proved by X-rays to have the ligands in a *trans* arrangement (Figure 1B).[4] To our knowledge, reported in the literature, there is only a restricted number of Pd^{II} or Pt^{II} carborane derivatives structurally well-characterized, for them there being no trace of attention given for their application in BNCT.[6] In the present work, once prepared, isolated, and structurally definitely characterized also the isomer *cis*-

Received: April 10, 2021

https://doi.org/10.1021/acs.inorgchem.1c01092
Inorg. Chem. XXXX, XXX, XXX−XXX

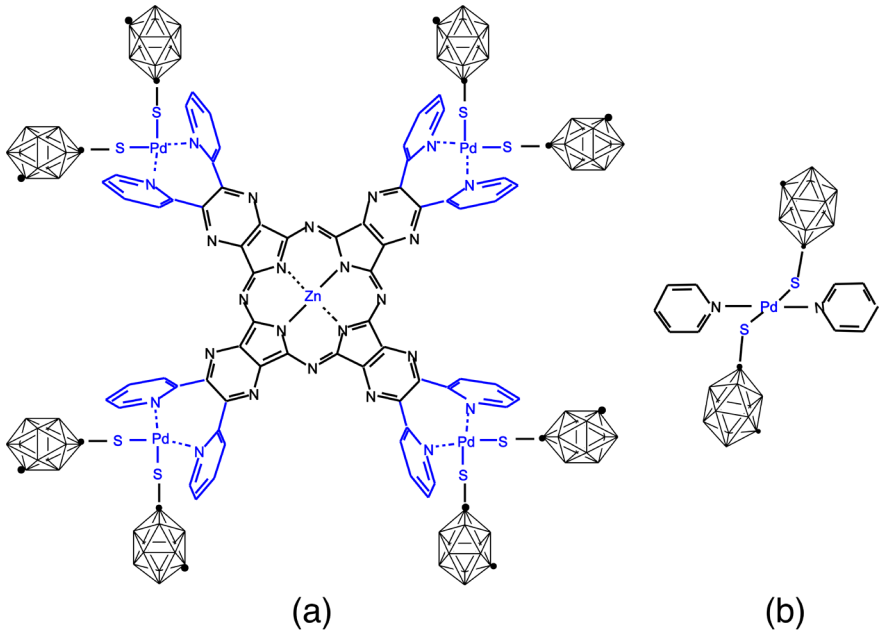

Figure 1. Schematic representation of the porphyrazine complexes of (a) general formula $[\{Pd(CBT)_2\}_4LM]\cdot xH_2O$ (L = 2,3-[5,6-di(2-pyridyl)pyrazino] porphyrazinato; M = $Mg^{II}(H_2O)$, Zn^{II}, Pd^{II}) and (b) of the *trans*-$[(py)_2Pd(CBT)_2]$ complex.

$[(bipy)Pd(CBT)_2]$ (bipy = 2,2′-bipyridyl), both the cited *trans* and *cis* potential BNCT agents have been studied, on the basis of their infrared (IR) and ultraviolet−visible light (UV-vis) spectral behavior. Noteworthy, a distinct UV-vis spectral feature is shown for the *cis* isomer, because of the presence in the region 400−500 nm of a broad absorption, absent instead in the spectrum of the *trans* complex; this fact is related to the occurrence in the *cis* structure of a vicinal arrangement of the two CBT groups. The ground-state molecular and electronic structure and the electronic absorption spectra of both species have been theoretically investigated by density-functional theory (DFT) and time-dependent density-functional theory (TDDFT) methods, both in the gas-phase and $CHCl_3$ solution. The observed tendency in pyridine solution of the process *cis*-$[(bipy)Pd(CBT)_2]$ → *trans*-$[(py)_2Pd(CBT)_2]$, from one side duplicates what observed for the above cited Zn^{II}CBT macrocycle $[\{Pd(CBT)_2\}_4LZn]\cdot xH_2O$ indicating also that the *cis*-$[(bipy)Pd(CBT)_2]$ species adequately models the $(\sim py)_2Pd(CBT)_2$ groups appended to the periphery of the above cited macrocycles.[4,5] The *cis* → *trans* conversion has been theoretically investigated by DFT calculations, both in the gas-phase and $CHCl_3$ solution.

EXPERIMENTAL SECTION

Solvents and reagents were commercially obtained and used as received unless otherwise specified. *m*-carborane-1-thiol (CBTH) was purchased from Katchem, Ltd. Pyridine was freshly distilled over BaO before use. Bis-benzonitrile Pd^{II} chloride, $[(C_6H_5CN)_2PdCl_2]$,[7] and the hydrated porphyrazine complex $[\{Pd(CBT)_2\}_4LZn]\cdot 17H_2O$ were obtained as reported elsewhere.[4]

Synthesis of *trans*-$[(py)_2PdCl_2]$. This complex has been prepared using a procedure slightly different from that previously reported.[8] $PdCl_2$ (52 mg, 0.29 mmol) was suspended in pyridine (10 mL) and the mixture was kept at room temperature under stirring for 2 h. The color of the solution changed from brown to light yellow. After separation of the brown residual $PdCl_2$ by settling, the suspension was centrifuged and the separated yellow solid material was washed with acetone and brought to constant weight under vacuum (10^{-2} mmHg) (42.6 mg, 0.123 mmol; yield 42%). Calcd for *trans*-$[(py)_2PdCl_2]$, $C_{10}H_{10}Cl_2N_2Pd$: C, 35.80; H, 3.00; N, 8.35; Pd, 31.72%. Found: C, 35.60; H, 2.92; N, 8.06; Pd 31.05%. IR (cm^{-1}): 3088 (vw), 3046 (vvw), 3023 (vw), 2985 (vvw), 1594 (m), 1561 (vvw), 1477 (m-w), 1445 (m-s), 1351 (vvw), 1236 (vw), 1209 (w), 1195 (vw), 1146 (w), 1073 (m-w), 1061 (w), 1046 (vvw), 1010 (vw), 971 (vvw), 935 (vvw), 862 (vvw), 757 (s), 682 (vs), 649 (vvw), 462 (w), 393 (m-w), 351 (m, ν_{Pd-Cl}), 266 (m-w). UV−vis spectral data (λ, nm (log ε)) in CH_3CN: 230 (4.37), 259 (3.85), 267 (3.68); in $CHCl_3$: 242 (4.19), 261 (3.88), 268 (3.74); in THF: 267 (4.20), 270 (3.94), 274 (3.61).

Synthesis of *cis*-$[(bipy)PdCl_2]$. This complex has been prepared using a procedure slightly different from that previously reported.[9] A solution of bipy (60 mg, 0.38 mmol) in MeOH (5 mL) and a solution of $(C_6H_5CN)_2PdCl_2$ (121 mg, 0.31 mmol) in the same solvent (5 mL) were mixed. The orange mixture formed immediately, after the mixing of the two solutions was kept in a refrigerator overnight. The resulting pink solid was separated by centrifugation, washed several times with MeOH and brought to a constant weight under vacuum (10^{-2} mmHg) (74.1 mg, 0.222 mmol; yield 58.5%). Calcd for *cis*-$[(bipy)PdCl_2]$, $C_{10}H_8Cl_2N_2Pd$: C, 36.01; H, 2.42; N, 8.40; Pd, 31.91%. Found: C, 35.88; H, 2.27; N, 8.31; Pd, 32.44%. IR (cm^{-1}): 3385 (vw), 3088 (w), 3067 (w), 3052 (w), 3029 (w-m), 3012 (w), 1594 (w), 1594 (m-s), 1556 (vw), 1488 (vw), 1460 (m-s), 1441 (vs), 1319 (vvw), 1422 (w-m), 1320 (w), 1309 (w-m), 1236 (w-m), 1157 (s), 1109 (w), 1065 (vw), 1054 (vvw), 1031 (w-m), 1017 (vw), 962 (vvw), 891 (vvw), 760 (vvs), 715 (m), 646 (vw), 483 (vvw), 408 (w), 341 (ν_{Pd-Cl}, s). UV−vis spectral data (λ, nm (log ε)) in CH_3CN: 259 (4.15), 305 (4.08), 316 (4.14); in $CHCl_3$: 265 (4.17), 307 (4.10), 316 (4.17); in THF: 307 (4.11), 316 (4.19).

Synthesis of *trans*-$[(py)_2Pd(CBT)_2]$. *Method (a).* Samples of this compound could be obtained from the porphyrazine macrocycle $[\{Pd(CBT)_2\}_4LZn]\cdot 17H_2O$ using a procedure reported elsewhere.[4]

Method (b). Alternatively, the complex could be prepared from *trans*-$[(py)_2PdCl_2]$ and *m*-carborane-1-thiol (CBTH) as follows: *trans*-$[(py)_2PdCl_2]$ (19.5 mg, 0.056 mmol) and *m*-carborane-1-thiol (59.7 mg, 0.339 mmol) were added to a small flask (10 mL) containing py (3 mL). The mixture was kept at 50 °C under stirring for 24 h. A color change from light to intense orange was observed. At the end of the reaction, the solution was transferred into a vessel and left to concentrate to air. After 4 days, yellowish crystals were isolated, washed with few drops of py and brought to constant weight under vacuum (10^{-2} mmHg) (14.0 mg, 0.023 mmol; yield 40%). Calcd for

https://doi.org/10.1021/acs.inorgchem.1c01092
Inorg. Chem. XXXX, XXX, XXX−XXX

trans-[(py)$_2$Pd(CBT)$_2$], $C_{14}H_{32}B_{20}N_2PdS_2$: C, 27.33; H, 5.24; N, 4.55; S, 10.42; Pd, 17.30%. Found: C, 27.16; H, 6.56; N, 4.42; S, 10.02; Pd, 18.18%. IR (cm^{-1}): 3060 (vvw), 3033 (vw), 2573 (vs), 1637 (vvw), 1594 (m-w), 1473 (w), 1441 (s), 1381 (vvw), 1343 (w), 1236 (vw), 1202 (m-w), 1148 (vvw), 1125 (vw), 1084 (vvw), 1063 (m-w), 1027 (vvw), 1012 (vvw), 996 (vw), 969 (w), 927 (vvw), 864 (m), 818 (vvw), 753 (m), 722 (m-w), 684 (m-s), 647 (vvw), 625 (vvw), 387 (vvw), 276 (vw). UV−visible spectral data (λ, nm (log ε)) in CH_3CN: 263 (3.79), 317 (3.80); in $CHCl_3$: 253 (4.19), 322 (4.36); in THF: 320 (4.12); in py: 320 (4.51).

Synthesis of *cis*-[(bipy)Pd(CBT)$_2$]. *Method (a).* The [{Pd(CBT)$_2$}$_4$LZn]·17H$_2$O complex (20.2 mg, 0.006 mmol) and bipy (18.4 mg, 0.118 mmol) were introduced in a small flask (10 mL) containing CH_3CN (2 mL). The mixture was kept at 70 °C under stirring for 24 h. After cooling to room temperature and centrifugation, the separated dark green solid was washed with a small amount of acetone and brought to constant weight under vacuum (10^{-2} mmHg) (3.8 mg, 6.20×10^{-3} mmol; yield 53%). The mother liquors, after concentration by exposition to air, led to the formation of orange crystals (6 mg, yield 41%). On the basis of elemental analysis, IR and UV-vis spectral data, the green solid compound was identified as the mononuclear complex [LZn], as expected. In turn, the orange crystals were identified by general characterization data and single-crystal X-ray analysis and as constituted by the complex *cis*-[(bipy)Pd(CBT)$_2$]. Calcd for *cis*-[(bipy)Pd(CBT)$_2$], $C_{14}H_{30}B_{20}N_2PdS_2$: C, 27.42; H, 4.93; N, 4.57; S, 10.46; Pd, 17.35%. Found: C, 27.85; H, 4.51; N, 5.31; S, 9.82; Pd, 18.09%. IR (cm^{-1}): 3107 (vw), 3059 (vw), 3039 (vw), 3028 (vw), 2585 (vs), 1586 (m), 1554 (vw), 1481 (vw), 1458 (m), 1435 (m-s), 1303 (w-m), 1270 (vw), 1238 (vw), 1163 (w), 1150 (w), 1125 (vw), 1098 (w), 1067 (vw), 1023 (w-m), 967 (w), 860 (m), 818 (vw), 759 (s), 722 (m-s), 653 (w), 636 (w), 414 (vw), 321 (w), 291 (w), 264 (w-m). UV−visible spectral data (λ, nm (log ε)) in CH_3CN: 307 (4.23), 315 (4.25), 343 (3.62), 452 (2.52); in $CHCl_3$: 250 (4.70), 308 (4.19), 356 (3.48), 450 (3.05); in THF: 248 (4.55), 307 (4.10), 316 (4.11), 355 (3.54), 446 (2.47).

Method (b). The *cis*-[(bipy)Pd(CBT)$_2$] complex could also be prepared as solvated (CH_3CN) species by reacting the *cis*-[(bipy)PdCl$_2$] complex with *m*-carborane-1-thiol according to the following procedure: *cis*-[(bipy)PdCl$_2$] (20 mg, 0.060 mmol) and *m*-carborane-1-thiol (63.46 mg, 0.36 mmol) were added to CH_3CN (3 mL) and the mixture was refluxed at 90 °C under stirring for 8 h. After cooling to room temperature, orange crystals were formed over 24 h. The crystals were separated from the solution by centrifugation, washed with MeOH and brought to constant weight under vacuum (10^{-2} mmHg) (5.4 mg, 8.25×10^{-3} mmol; yield 13.8%). Calcd for *cis*-[(bipy)Pd(CBT)$_2$]·CH_3CN, $C_{16}H_{33}B_{20}N_3PdS_2$: C, 29.37; H, 5.08; N, 6.42; S, 9.80; Pd, 16.27%. Found: C, 29.21; H, 4.98; N, 6.72; S, 9.43; Pd, 15.50%.

X-ray Diffraction Data. Data on the complex *cis*-[(bipy)Pd(CBT)$_2$] were collected on a Bruker APEX-II CCD diffractometer using graphite-monochromatized Mo Kα radiation at 294(2) K. Unit-cell parameters were determined by using the APEX2 program.[10] Data reduction was performed by the SAINT program.[11] Correction for absorption was performed using the SADABS program.[12] The function minimized during least-squares refinement was $\sum w(\Delta F^2)$. Anomalous scattering correction was included in the structure factor calculation. The structure was solved by direct methods using SHELXT.[7] Refinement was done anisotropically by full matrix least-squares for all non-hydrogen atoms using SHELXL-2014/755.[12] The hydrogen atoms were placed in idealized calculated positions with C−H= 0.93−1.10 Å, B−H = 1.10 Å, and refined using a riding model approximation, with U_{iso}(H) = 1.2 U_{eq}(C, B).

Quantum Chemical Calculations. The calculations were performed with ADF (Amsterdam Density Functional),[13] using the range-separated (RS) hybrid CAMY-B3LYP functional.[14] The calculations included relativistic effects through the Zero-Order Regular Approximation (ZORA).[15] In the calculations of the ground-state molecular and electronic structure and the electronic absorption spectra of the *cis*-[(bipy)Pd(CBT)$_2$] and *trans*-[(py)$_2$Pd(CBT)$_2$] complexes the all-electron ZORA TZ2P basis set that is an uncontracted triple-ζ STO basis with two polarization functions was employed.[16] Geometry optimization of the complexes was performed in the gas phase and in $CHCl_3$ solution, where, according to the electronic absorption spectroscopic studies, both complexes are stable. The optimizations were performed starting from the X-ray structures without symmetry constraint yielding molecular structures of C_2 and C_i symmetry for the *cis*-[(bipy)Pd(CBT)$_2$] and *trans*-[(py)$_2$Pd(CBT)$_2$] complexes, respectively.

However, to retain the same orientation of the *x*, *y*, *z* axes as in the *trans*-[(py)$_2$Pd(CBT)$_2$] complex, the calculations of the ground and excited states of the *cis*-[(bipy)Pd(CBT)$_2$] complex have been performed in C_1 symmetry.

The effects of the solvent ($CHCl_3$) on the molecular and electronic structure, and the lowest excited states were modeled through the conductor-like continuum solvent model (COSMO).[17]

The *cis*-[(bipy)Pd(CBT)$_2$] → *trans*-[(py)$_2$Pd(CBT)$_2$] conversion reaction was theoretically studied in the gas phase using the all-electron ZORA TZP basis set that is an uncontracted triple-ζ STO basis with one polarization function.[16] Geometry optimizations of all the species involved in the reaction were performed without symmetry constraints. The subsequent frequency calculations verified that all local minima had only real frequencies and that transition states were characterized by single imaginary frequency. The zero-point energies (ZPE) were obtained from these frequency calculations. The effects of the solvent ($CHCl_3$) on the energies were evaluated through single-point calculations using the COSMO model.[17] If not otherwise specified, the energies reported for the species involved in the *cis*-[(bipy)Pd(CBT)$_2$] → *trans*-[(py)$_2$Pd(CBT)$_2$] conversion reaction include both ZPE correction and solvation effects.

A preliminary study of the reaction potential energy surface (PES) was performed at a lower level of theory using the B3LYP exchange-correlation functional,[18] in combination with the def2-SV(P) basis set for all atoms[19] and effective core potential for Pd.[20] The calculations, referred to as B3LYP/def2-SV(p) in the paper, were performed in the gas phase with Gaussian09 Version D.01[21] and included scans of the relaxed PEs with location of minima and saddle points.

To analyze and quantify the electronic factors governing the formation of the trigonal bipyramidal transition state complex upon attack of pyridine to *cis*-[(bipy)Pd(CBT)$_2$], we made use of the energy-partitioning scheme implemented in ADF, which was originally developed for Hartree−Fock wave functions by Morokuma[22] and modified for the relaxation energy (or orbital interaction term) by Ziegler and Rauk.[23] The energy decomposition analysis (EDA) is for the interaction of the entering pyridine ligand and the *cis*-[(bipy)Pd(CBT)$_2$] along the Pd−Npy reaction coordinate. The interaction energy ΔE_{int} is analyzed in the framework of the Kohn−Sham (KS) MO model, using a Morokuma-type decomposition into the steric interaction term, ΔE^0, and the (attractive) orbital interaction term ΔE_{oi}.[24]

$$\Delta E_{int} = \Delta E^0 + \Delta E_{oi} \quad (1)$$

In turn, the ΔE^0 term comprises the electrostatic interaction, ΔV_{elstat}, and the Pauli repulsion (or exchange repulsion):

$$\Delta E^0 = \Delta V_{elstat} + \Delta E_{Pauli} \quad (2)$$

The term ΔV_{elstat} corresponds to the classical electrostatic interaction between the unperturbed charge distributions of the fragments and is usually attractive. The second term in eq 2), ΔE_{Pauli}, refers to the repulsive interactions between the fragments, which are caused by the fact that two electrons with the same spin cannot occupy the same region in space. ΔE_{Pauli} is calculated by enforcing the KS determinant of the superimposed fragments to obey the Pauli principle by antisymmetrization and renormalization. The ΔE_{Pauli} term consists of the three- and four-electron destabilizing interactions between occupied orbitals and corresponds to the intuitive concept of steric repulsion[25] that is widely used in chemistry. The stabilizing orbital interaction term, ΔE_{oi}, is calculated in the final step of the energy

https://doi.org/10.1021/acs.inorgchem.1c01092
Inorg. Chem. XXXX, XXX, XXX−XXX

partitioning analysis when the KS orbitals relax to the fully converged ground-state wave function of the total molecule. This term accounts for charge transfer (interaction between occupied orbitals on one molecular fragment and unoccupied orbitals on the other), and polarization (empty/occupied orbital mixing on one fragment).[22]

Physicochemical Measurements. IR spectra were recorded on a Varian FT-IR 660 in the range of 4000−250 cm^{-1} (KBr pellets or nujol mulls between CsI disks). UV-vis solution spectra were recorded with a Varian Cary 5E spectrometer, using 1 cm quartz cuvettes. Elemental analyses for C, H, N, and S were provided by the "Servizio di Microanalisi" at the Dipartimento di Chimica, Università "La Sapienza" (Rome), on an EA 1110 CHNS-O instrument. The ICP PLASMA Pd analyses were performed on a Varian Vista MPX CCD simultaneous ICP-OES.

RESULTS AND DISCUSSION

Synthesis and Characterization. As anticipated in the Introduction, the *trans*-$[(py)_2Pd(CBT)_2]$ complex (Figure 1b) was originally obtained as a byproduct of the reaction of $[\{Pd(CBT)_2\}_4LZn]\cdot xH_2O$ (Figure 1a) with pyridine.[4] In the present work, the same species has been also obtained upon reaction of the *trans*-$[(py)_2PdCl_2]$ with *m*-carborane-1-thiol, but in significantly larger amount. The *cis*-$[(bipy)Pd(CBT)_2]$ species, which models the $(\sim py)_2Pd(CBT)_2$ groups appended to the periphery of the $[\{Pd(CBT)_2\}_4LM]\cdot xH_2O$ complexes,[4] was obtained through the same two pathways (Methods (a) and (b) in the Experimental Section) as the *trans*-$[(py)_2Pd(CBT)_2]$ complex, except that bipy was used instead of py and the reactions were conducted in CH_3CN rather than in pyridine.

The IR spectra of *cis*-$[(bipy)PdCl_2]$, *cis*-$[(bipy)Pd(CBT)_2]$ and *trans*-$[(py)_2Pd(CBT)_2]$ are shown in Figure S1 in the Supporting Information. The spectrum of *cis*-$[(bipy)PdCl_2]$ from which the related CBT derivative *cis*-$[(bipy)Pd(CBT)_2]$ is obtained shows the clean stretching $\nu_{(Pd-Cl)}$ at 341 cm^{-1} absent in the spectrum of *cis*-$[(bipy)Pd(CBT)_2]$, as expected. The IR spectra of both *cis* and *trans* CBT derivatives show a narrow low intensity peak at 3039/3033 cm^{-1} and a very intense peak at 2585/2573 cm^{-1} assigned to the C−H and the B−H stretching vibrations of the *m*-carborane cage, respectively.[26]

X-ray Structure. Table 1 summarizes experimental and structure refinement parameters of the *cis*-$[(bipy)Pd(CBT)_2]$ complex and, for comparison purpose, of the previously structurally characterized *trans*-$[py_2Pd(CBT)_2]$ analogue. The molecular structures of the two complexes are displayed in Figure 2, while selected bond distances and angles are gathered in Table 2.

The structure of *cis*-$[(bipy)Pd(CBT)_2]$ consists of mononuclear discrete molecules with the metal displaying a slightly distorted square planar coordination geometry. The *m*-carborane groups are oriented in opposite directions, with respect to the substantially planar coordination plane (root mean square (rms) = 0.0117 Å; maximum displacement = 0.017(5) Å for atom N2). The N1/C1—C5 and N2/C6—C10 pyridine rings of the bipy ligand are almost coplanar (dihedral angle = 3.89(19)°) and form dihedral angles of 6.03(15) and 6.67(14)° with the mean plane through the N_2S_2 donor set of atoms. The S−C bond distances (mean value 1.790(4) Å) are not significantly different from those observed in *trans*-$[(py)_2Pd(CBT)_2]$ (Table 2), whereas the Pd−S (mean value = 2.284(5) Å) and Pd−N (mean value = 2.088(7) Å) bond lengths are slightly shorter and longer, respectively. As observed for *trans*-$[(py)_2Pd(CBT)_2]$,[4] in the crystal packing the molecules interact only through van der Waals forces, no hydrogen bonding, C−H···π contacts or $\pi\cdots\pi$ interactions are observed (Figure S2 in the Supporting Information).

Table 1. Experimental Data for the X-ray Diffraction Study on the Crystalline Compounds *trans*-$[(py)_2Pd(CBT)_2]$[a] and *cis*-$[(bipy)\ Pd(CBT)_2]$

	trans-$[(py)_2Pd(CBT)_2]$	*cis*-$[(bipy)\ Pd(CBT)_2]$
formula	$C_{14}H_{32}B_{20}N_2PdS_2$	$C_{14}H_{30}B_{20}N_2PdS_2$
formula weight	615.13	613.12
crystal habit	needle	fragment
crystal color	yellow	orange
crystal dimension, mm	0.01 × 0.02 × 0.08	0.08 × 0.16 × 0.26
crystal system	monoclinic	orthorhombic
space group	$P2_1/c$	$P2_12_12_1$
cell parameters:		
a, Å	7.4049(18)	9.722(4)
b, Å	21.154(5)	14.180(6)
c, Å	9.660(2)	20.379(8)
α, °	90	
β, °	100.015(4)	
γ, °	90	
V, Å^3	1490.1(6)	2809(2)
Z	2	4
D_{calc}, Mg m^{-3}	1.371	1.450
linear absorption coefficient, mm^{-1}	0.775	0.822
diffractometer	Bruker APEX-II CCD	Bruker APEX-II CCD
temperature, K	294(2)	294(2)
radiation, Å	0.71073	0.71073
data collection range of 2θ, °	1.9−25.5	1.75−25.25
reflections measured	$\pm h, \pm k, \pm l$	$\pm h, \pm k, \pm l$
total data collected	12769	29212
unique total data	2768	5070
unique observed data	1742	4271
criterion for observation	$I > 2\sigma(I)$	$I > 2\sigma(I)$
unique data used in the refinement (NO)	2768	5070
number of parameters refined (NV)	178	352
overdetermination ratio (NO/NV)	15.6	14.4
transmission coefficients	0.610−0.745	0.536−0.745
$R = \sum\|\Delta F\|/\sum\|F_o\|$[b]	0.052	0.037
$wR^2 = [\sum w\|\Delta F^2\|^2/\sum w\|F_o^2\|^2]1/2$[c]	0.127	0.087
GOF = $[\sum w\|\Delta F^2\|^2/(NO - NV)]1/2$	1.034	1.030
largest shift/esd, final cycle	<0.001	<0.001
largest peak, e/Å^3	0.08	0.58

[a]Data from ref.[2] [b]Calculated on the unique observed data. [c]Calculated on the unique data used in the refinement.

Electronic Absorption Spectra. The *cis* and *trans* CBT derivatives are fairly well soluble in $CHCl_3$, CH_3CN and THF. Their UV−vis spectral data in these solvents are gathered in Table 3, where, for comparison purposes, those of the of *cis*-$[(bipy)PdCl_2]$ complex are also reported. According to the data in the table, the salient features of the UV−vis spectra of all three complexes show only a modest sensitivity to the nature of the solvent.

As inferred from Figure 3 where the quantitative UV−vis spectra in $CHCl_3$ of the *cis*-$[(bipy)Pd(CBT)_2]$ and *trans*-$[(py)_2Pd(CBT)_2]$ complexes are displayed, the *trans* complex

https://doi.org/10.1021/acs.inorgchem.1c01092
Inorg. Chem. XXXX, XXX, XXX−XXX

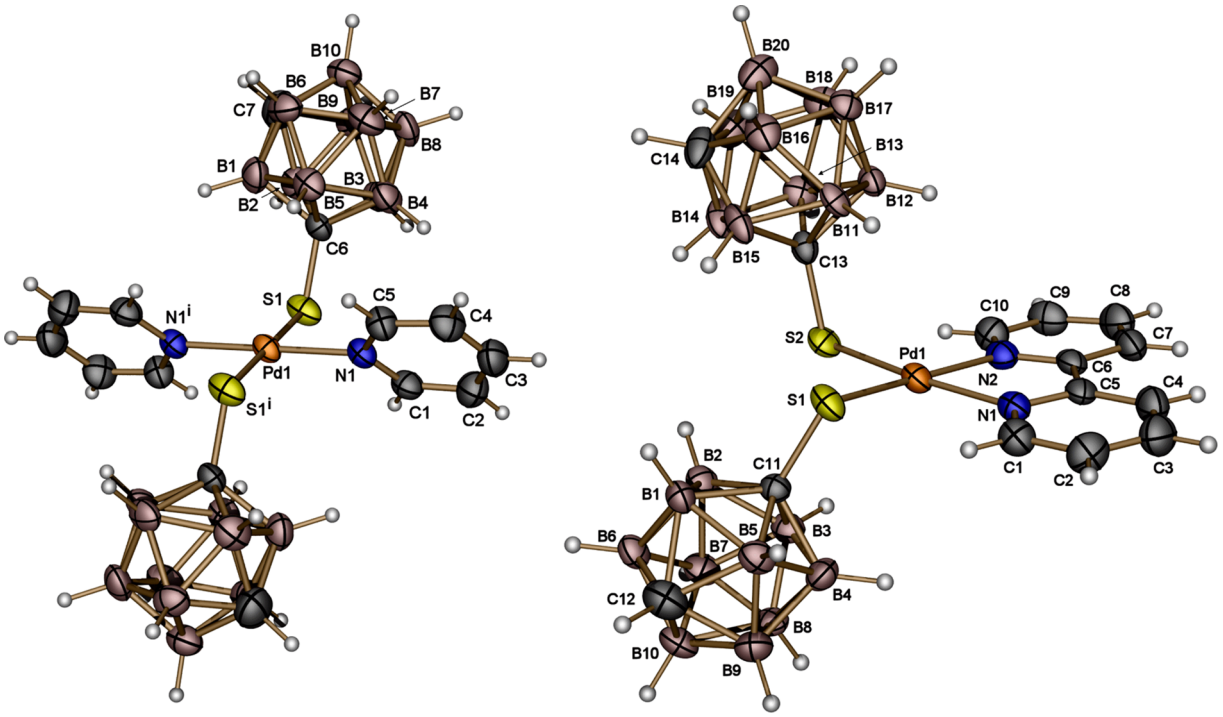

Figure 2. Molecular structure of *trans*-[$(py)_2Pd(CBT)_2$] (left) and *cis*-[(bipy)$Pd(CBT)_2$] (right) and with displacement ellipsoids drawn at the 40% probability level. The $S1^i$ and $N1^i$ atoms as well as those unlabeled of the *trans*-[$(py)_2Pd(CBT)_2$] complex have been generated by the transformation $1 - x$, $1 - y$, $1 - z$.

Table 2. Selected Bond Distances and Angles for *trans*-[$(py)_2Pd(CBT)_2$] and *cis*-[(bipy)$Pd(CBT)_2$]

trans-[$(py)_2Pd(CBT)_2$][a]			
Bond Distances (Å)			
Pd1—S1	2.3419(14)	S1—C6	1.789(5)
Pd1—N1	2.039(4)		
Bond Angles (°)			
N1—Pd1—S1	90.63(12)	N1—Pd1—$S1^i$	89.37(12)
S1—Pd1—$S1^i$	180	N1—Pd1—$N1^i$	180
symmetry code: (i) $1 - x$, $1 - y$, $1 - z$			
cis-[(bipy)$Pd(CBT)_2$]			
Bond Distances (Å)			
Pd1—S1	2.2893(19)	Pd1—N2	2.094(5)
Pd1—S2	2.2800(18)	S1—C11	1.794(6)
Pd1—N1	2.081(5)	S2—C13	1.786(6)
Bond Angles (°)			
S1—Pd1—S2	90.42(7)	S2—Pd1—N2	95.33(15)
S1—Pd1—N1	95.76(15)	N1—Pd1—N2	78.4(2)
S1—Pd1—N2	173.64(15)	Pd1—S1—C11	109.0(2)
S2—Pd1—N1	173.57(15)	Pd1—S2—C13	105.56(19)

[a]Data taken from ref 2.

shows an intense and substantially symmetric absorption peaking at 322 nm, followed at higher energy by a less intense, broad shoulder with maximum at 253 nm. Quite different is the spectral profile of the *cis*-[(bipy)$Pd(CBT)_2$] complex. Similar to the trans, this complex shows a rather intense absorption in the near UV, which is, however, significantly less intense than in the *trans* complex and shifted to higher energy by 14 nm (308 vs 322 nm). The 308 nm band is followed at higher energy by a much more intense and asymmetric absorption band with a maximum at 250 nm. Moreover, the cis complex shows a very broad and weak absorption in the 330–550 nm region, with detectable features at 356 and 450 nm (see the inset of Figure 3).

We note that position and intensity of the 450 nm feature are consistent with those exhibited by the absorption appearing in the 400–500 nm region of the spectra of the [{Pd-$(CBT)_2$}$_4$LM]·xH_2O pentanuclear complexes[4] and associated with the presence of the peripheral $(\sim py)_2Pd(CBT)_2$ groups. The band appearing in the 330–550 nm region of the *cis*-[(bipy)$Pd(CBT)_2$] complex is absent in the spectrum of the bipy analog *cis*-[(bipy)$PdCl_2$], suggesting that it is somewhat related to the electronic structure characteristics exerted by the CBT groups when they are in a cis arrangement. The UV-vis spectral features of the *cis*-[(bipy)$Pd(CBT)_2$] complex observed in $CHCl_3$, CH_3CN and THF remain substantially the same in DMF, DMSO, and even in a DMSO/H_2O mixture (see Table 3), a behavior that can be interesting from the perspective of testing the potential of this complex as an anticancer BNCT agent.

***cis*-[(bipy)$Pd(CBT)_2$] → *trans*-[$(py)_2Pd(CBT)_2$] Conversion.** The *cis*-[(bipy)$Pd(CBT)_2$] is stable in $CHCl_3$ solution. However, when an excess of pyridine is added to the $CHCl_3$ solution of the complex at room temperature and *in darkness* (molar ratio *cis*-[(bipy)$Pd(CBT)_2$]:py = 1:2080), its UV–vis spectrum slowly changes, assuming the profile of the *trans*-[$(py)_2Pd(CBT)_2$] species (Figure 4), and the solution turns yellow. A single isosbestic point is observed at 360 nm.

This spectral evolution suggests that the *cis*-[(bipy)Pd-$(CBT)_2$] complex, upon reaction with pyridine, has converted to the *trans*-[$(py)_2Pd(CBT)_2$] species, releasing the bipy ligand, according to the reaction

$$cis\text{-}[(bipy)Pd(CBT)_2] + 2py \rightarrow trans\text{-}[(py)_2Pd(CBT)_2] + bipy$$

Based on the ε values in $CHCl_3$ of both complexes, it could be concluded that the conversion is complete after ~18 h. To

https://doi.org/10.1021/acs.inorgchem.1c01092
Inorg. Chem. XXXX, XXX, XXX–XXX

Table 3. UV-vis Spectral Data of *cis*-[(bipy)Pd(CBT)$_2$], *cis*-[(bipy)PdCl$_2$], and *trans*-[(py)$_2$Pd(CBT)$_2$] in Different Solvents

solvent	λ, nm (log ε)				
		cis-[(bipy)Pd(CBT)$_2$]			
$CHCl_3$	250 (4.70)	308 (4.19)		356 (3.48)	450 (3.05)
CH_3CN		307 (4.23)	315 (4.25)	343 (3.62)	452 (2.52)
THF	248 (4.55)	307 (4.10)	316 (4.11)	355 (3.54)	446 (2.47)
DMF	268 (4.44)	309 (4.19)	317 (4.15)	352 (3.50)	455 (2.56)
DMSO	261 (4.64)	311 (4.29)	323 (4.21)	362 (3.54)	439 (2.98)
DMSO/H_2O 10%	259 (4.51)	310 (4.10)	321 (4.04)	354 (3.44)	444 (3.02)
		cis-[(bipy)PdCl$_2$]			
$CHCl_3$	265 (4.17)	307 (4.10)	316 (4.17)		
CH_3CN	259 (4.15)	305 (4.08)	316 (4.14)		
THF		307 (4.11)	316 (4.19)		
		trans-[(py)$_2$Pd(CBT)$_2$]			
$CHCl_3$	253 (4.19)		322 (4.36)		
CH_3CN[a]	263 (3.79)		317 (3.80)		
THF			320 (4.12)		
py			320 (4.51)		

[a]Data from ref 2.

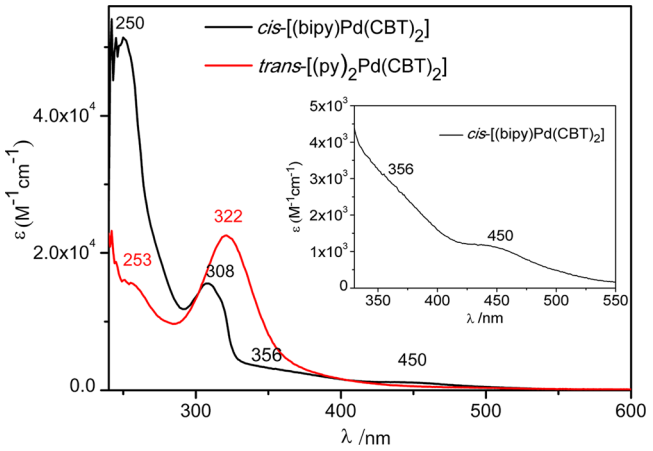

Figure 3. Quantitative UV-vis spectra in $CHCl_3$ of *cis*-[(bipy)Pd(CBT)$_2$] (black line) and *trans*-[(py)$_2$Pd(CBT)$_2$] (red line). The inset shows the spectrum of *cis*-[(bipy)Pd(CBT)$_2$] enlarged in the range of 330−550 nm.

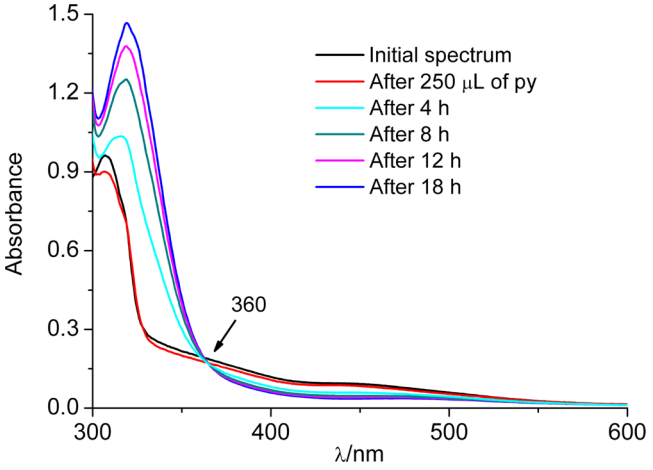

Figure 4. Evolution of the UV-vis spectrum of the *cis*-[(bipy)Pd(CBT)$_2$] complex in $CHCl_3$ upon addition of an excess of pyridine.

definitively assess the chemical identity of the formed species, the *cis*-[(bipy)Pd(CBT)$_2$] complex was reacted with pyridine at 50 °C (to speed up the reaction). X-ray analysis of the yellow crystals isolated from the pyridine solution confirmed they where constituted by the *trans*-[(py)$_2$Pd(CBT)$_2$] complex.

DFT Calculations of the Molecular and Electronic Structure. The relevant bond parameters of the *trans* and *cis* CBT derivatives computed in the gas phase and in $CHCl_3$ solution are reported in Table 4, together with the corresponding experimental data.

As inferred from the calculated bond parameters, the gas phase and $CHCl_3$ solution structures are almost identical and are very close to the experimental solid-state molecular structure, indicating that they are scarcely influenced by the environment. The calculations well reproduce the observed elongation of the Pd−N bonds and concomitant shortening of the Pd−S bonds upon going from the *trans*-[(py)$_2$Pd(CBT)$_2$] to the *cis*-[(bipy)Pd(CBT)$_2$] complex, a behavior that is most likely related to a significant trans influence of the thiolate ligands on the Pd−N bonds. Worth noting, in the *cis*-[(bipy)PdCl$_2$] complex, the Pd−N bonds are significantly shorter than in the analogous *cis*-[(bipy)Pd(CBT)$_2$] complex, 2.017(2) A (ref 5) vs 2.088(5) A, which is consistent with the chloride ligands having a weaker trans influence than the thiolate ligands.

The highest occupied and lowest unoccupied one-electron levels of the investigated complexes are shown in Figure 5 where the relevant molecular orbitals are also displayed.

Considering first the *trans*-[(py)$_2$Pd(CBT)$_2$] complex, the three highest occupied levels, the 79a$_g$ (HOMO), 75a$_u$ and 74a$_u$, are largely located on the sulfur lone pairs (S$_{lp}$), the metal orbitals contributing to the first and to the last with only a minor percentage. The Pd 4d$_{x^2-y^2}$ orbital contributes to some extent (8%) to the HOMO where it sets up a π-in plane antibonding interaction with the sulfur lone pairs (see the plot of the HOMO in Figure 5). In turn, the Pd 5p$_x$ and 5p$_y$ (Pd 5p$_\sigma$) empty orbitals mix in bonding fashion with the sulfur lone pair combination of A_u symmetry, the 74a$_u$. According to the Mulliken gross population of the metal orbitals, due to this σ-bonding interaction, the Pd 5p$_\sigma$ orbitals acquire 0.42 electrons. The highest occupied 4d levels are the 78a$_g$ (4d$_{z^2}$) and the closely lying 77a$_g$ and 76a$_g$ (4d$_\pi$). The former is largely (52%) 4d$_{z^2}$ with some (10%) 5s character and is destabilized by

https://doi.org/10.1021/acs.inorgchem.1c01092
Inorg. Chem. XXXX, XXX, XXX−XXX

Table 4. Selected Bond Lengths (Å) and Angles (deg) Calculated for *trans*-[(py)$_2$Pd(CBT)$_2$] and *cis*-[(bipy)Pd(CBT)$_2$] in the Gas Phase and in $CHCl_3$ Solution Are Compared to the Experimental Data

	trans-[(py)$_2$Pd(CBT)$_2$]			*cis*-[(bipy)Pd(CBT)$_2$]		
	gas phase	$CHCl_3$	expt[a]	gas phase	$CHCl_3$	expt[b]
			Bond Lengths (Å)			
Pd–N	2.062	2.055	2.039(4)	2.132	2.116	2.088(5)[c]
Pd–S	2.374	2.377	2.3419(14)	2.305	2.314	2.2850(18)[c]
			Bond Angles (°)			
$(N–Pd–N)_{op}$[d]	180.0	180.0	180.0			
$(N–Pd–N)_{ad}$[e]				77.3	78.0	78.4(2)
$(S–Pd–S)_{op}$[d]	180.0	180.0	180.0			
$(S–Pd–S)_{ad}$[e]				90.8	90.0	90.42(7)
$(N–Pd–S)_{op}$[d]				173.2	173.8	173.61(15)[c]
$(N–Pd–S)_{ad}$[e]	90.0	90.0	90.63(12)	95.9	95.9	95.55(15)[c]

[a]X-ray data taken from ref 4. [b]X-ray data, this work. [c]Average value. [d]Opposite ligands. [e]Adjacent ligands.

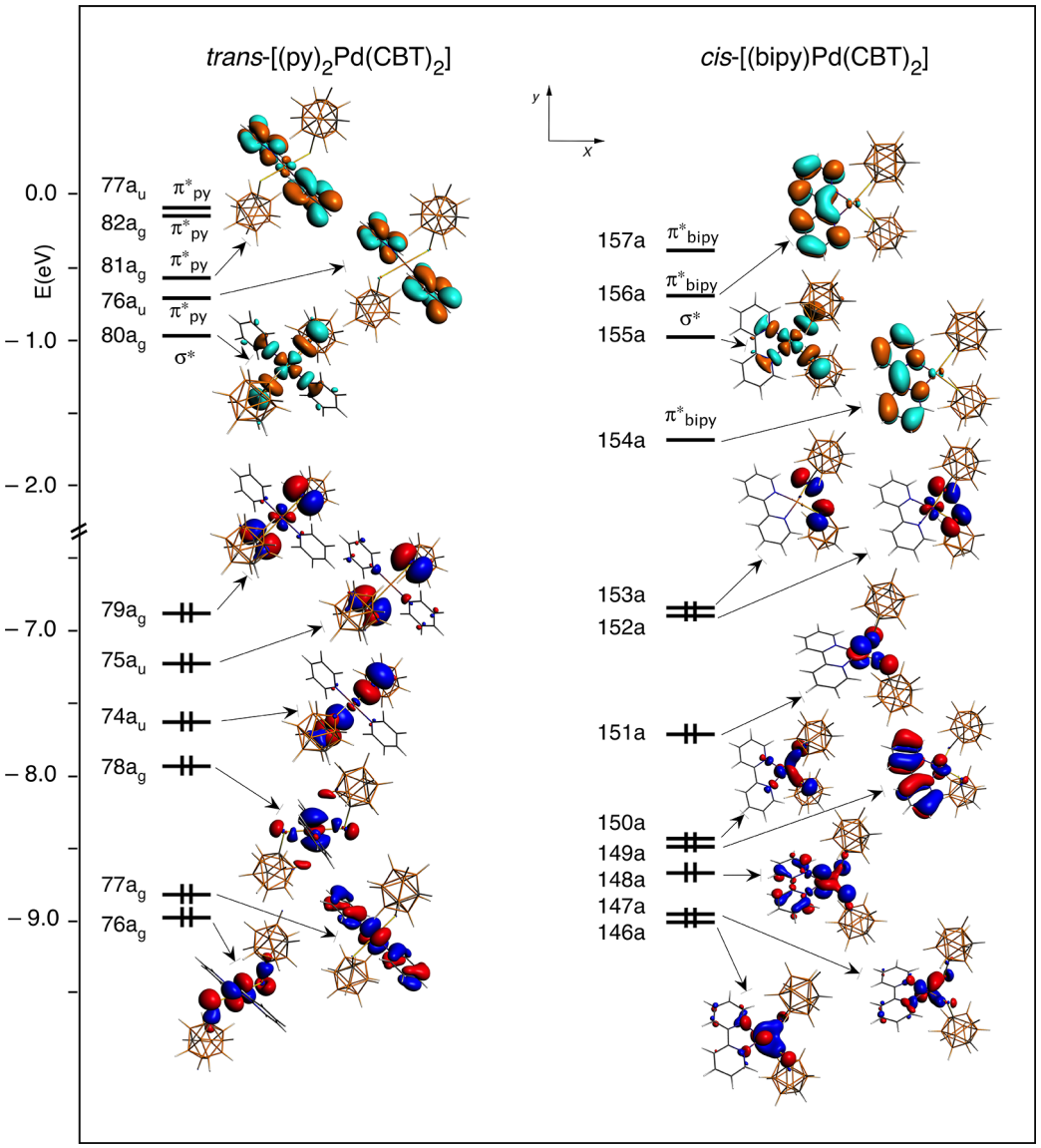

Figure 5. DFT/ZORA/CAMY-B3LYP/TZ2P/COSMO energy level diagram and relevant molecular orbitals of *trans*-[(py)$_2$Pd(CBT)$_2$] and *cis*-[(bipy)Pd(CBT)$_2$] in $CHCl_3$ solution. The contour values are ±0.04 e/au^3.

antibonding with the sulfur and nitrogen lone pairs (N_{lp}). The mixing of the 5s into the $4d_{z^2}$ causes a charge transfer of 0.20 electrons from the latter to the former. This implies that the 5s population of 0.36 electrons does not faithfully represent the amount of charge coming out of the sulfur lone pairs and, to a lesser extent, the nitrogen lone pairs. The $4d_{\pi}$ orbitals are

https://doi.org/10.1021/acs.inorgchem.1c01092
Inorg. Chem. XXXX, XXX, XXX–XXX

Table 5. Vertical Excitation Energies (E_{va}) and Oscillator Strengths (f) Computed in $CHCl_3$ Solution for the Spin- and Symmetry-Allowed Excited States of *trans*-$[(py)_2Pd(CBT)_2]$ Contributing to the UV-vis Spectral Region Are Compared to the Experimental Data

state[a]	composition (%)	character	E_{va} (eV)/λ (nm)	f	λ_{max}[b] (nm)
1^1A_u	$75a_u \rightarrow 80a_g$ (94)	$S_{lp} \rightarrow \sigma^*$	3.51/353	0.018	
3^1A_u	$74a_u \rightarrow 80a_g$ (94)	$S_{lp} \rightarrow \sigma^*$	4.18/297	0.963	322
4^1A_u	$75a_u \rightarrow 81a_g$ (91)	$S_{lp} \rightarrow \pi^*_{py}$	4.60/270	0.027	
7^1A_u	$79a_g \rightarrow 77a_u$ (94)	$S_{lp} \rightarrow \pi^*_{py}$	4.84/256	0.095	253
8^1A_u	$74a_u \rightarrow 81a_g$ (98)	$S_{lp} \rightarrow \pi^*_{py}$	4.94/251	0.085	
9^1A_u	$75a_u \rightarrow 82a_g$ (94)	$S_{lp} \rightarrow \pi^*_{py}$	5.23/237	0.104	

[a]Only the excited states with $f \geq 0.01$ are reported. [b]$CHCl_3$ solution spectrum of *trans*-$[(py)_2Pd(CBT)_2]$; data obtained from this work.

Table 6. Vertical Excitation Energies (E_{va}) and Oscillator Strengths (f) Computed in $CHCl_3$ solution for the Spin-Allowed Excited States of *cis*-$[(bipy)Pd(CBT)_2]$ Contributing to the UV-vis Spectral Region Are Compared to the Experimental Data

state[a]	composition (%)	character	E_{va} (eV)/λ (nm)	f	λ_{max}[b] (nm)
2^1A	$153a \rightarrow 155a$ (95)	$S_{lp} \rightarrow \sigma^*$	3.00/413	0.019	450
3^1A	$151a \rightarrow 155a$ (75)	$4d_{z^2}$, $S_{lp} \rightarrow \sigma^*$	3.12/398	0.034	356
	$148a \rightarrow 155a$ (12)	$4d_{xz} \rightarrow \sigma^*$			
8^1A	$147a \rightarrow 155a$ (45)	$4d_{xz}$, $S_{lp} \rightarrow \sigma^*$	3.77/320	0.020	
	$150a \rightarrow 155a$ (45)	S_{lp}, $4d_{xz} \rightarrow \sigma^*$			
11^1A	$149a \rightarrow 154a$ (91)	$\pi_{bipy} \rightarrow \pi^*_{bipy}$	4.32/287	0.229	308
12^1A	$150a \rightarrow 154a$ (86)	S_{lp}, $4d_{xz} \rightarrow \pi^*_{bipy}$	4.43/280	0.159	
13^1A	$148a \rightarrow 154a$ (83)	$4d_{xz}$, $\pi^*_{bipy} \rightarrow \pi^*_{bipy}$	4.51/275	0.224	
16^1A	$147a \rightarrow 154a$ (74)	$4d_{xz}$, $S_{lp} \rightarrow \pi^*_{bipy}$	4.86/255	0.122	250
17^1A	$146a \rightarrow 155a$ (29)	$4d_{yz}$, $4d_{z^2} \rightarrow \sigma^*$	4.91/253	0.401	
	$151a \rightarrow 156a$ (17)	$4d_{z^2}$, $S_{lp} \rightarrow \pi^*_{bipy}$			
	$151a \rightarrow 155a$ (10)	$4d_{z^2}$, $S_{lp} \rightarrow \sigma^*$			
	$148a \rightarrow 155a$ (10)	$4d_{xz} \rightarrow \sigma^*$			
18^1A	$151a \rightarrow 156a$ (70)	$4d_{z^2}$, $S_{lp} \rightarrow \pi^*_{bipy}$	4.92/252	0.108	
	$146a \rightarrow 155a$ (10)	$4d_{yz}$, $4d_{z^2} \rightarrow \sigma^*$			

[a]Only the excited states with $f \geq 0.01$ are reported. [b]$CHCl_3$ solution spectrum of *cis*-$[(bipy)Pd(CBT)_2]$; data obtained from this work.

heavily mixed with the pyridine π MOs in the $77a_g$ and with the sulfur lone pairs in the $76a_g$. Except for its modest involvement in the HOMO, the Pd $4d_{x^2-y^2}$ is basically a nonbonding orbital and lies lower in energy. Among the unoccupied orbitals, there is the Pd $4d_{xy}$ (42%) that is destabilized by σ antibonding with the sulfur lone pairs (32%) and nitrogen lone pairs (13%). The pertinent MO, the $80a_g$-LUMO, is denoted in the level scheme as σ^*. This Pd−ligands σ-interaction is quite strong, as inferred from the considerable charge acquired by the Pd $4d_{xy}$ (1.0 electron). The levels above the LUMO are pure π^* orbitals of the pyridine ligands (π^*_{py}).

Comparing the level schemes of the *trans*-$[(py)_2Pd(CBT)_2]$ and *cis*-$[(bipy)Pd(CBT)_2]$ complexes in Figure 5, it is apparent that the replacement of the two pyridines by the bipy ligand and the *cis* arrangement of the CBT ligands have appreciable effects on the energy and composition of the frontier MOs. First, the two highest occupied levels of the *cis* complex, the nearly degenerate 153a and 152a, which also are largely sulfur lone pair orbitals, lie higher in energy than in the *trans* species. Second, a quite large energy gap separates these MOs from the 151a (HOMO−2). Unlike in the *trans* complex the HOMO−2 has a mixed sulfur/metal character, the S_{lp} being heavily mixed in antibonding fashion with the Pd $4d_{z^2}$ (37%) and Pd 5s (11%) orbitals. Because of this mixing, the 5s acquires 0.22 electrons. The bonding counterpart of the 151a is the 148a where, in the place of the Pd 5s enters the Pd $4d_{yz}$ (24%). Most of this metal orbital (40%) is found in the 146a, where it mixes with the sulfur and nitrogen lone pairs in bonding and antibonding fashion, respectively. A minor percentage (10%) of the Pd $4d_{yz}$ is found in the 149a that is basically a bipy π-orbital (π_{bipy}) and, as such, has no counterpart in the trans complex. The Pd $4d_{xz}$ contributes to the 150a (24%) and the lower lying 147a (49%). In both MOs, the Pd $4d_{xz}$ sets up a bonding interaction with the sulfur lone pairs and antibonding interaction with the nitrogen lone pairs. Besides the Pd 5s, also the Pd $5p_\sigma$ orbitals are involved in the metal−ligand interactions. According to the Mulliken gross population, the charge of the Pd $5p_x$ and $5p_y$ amounts, indeed, to 0.20 and 0.19 electrons, respectively.

As in the *trans* complex, the Pd $4d_{xy}$ (43%) is destabilized by σ antibonding with the sulfur (33%) and nitrogen (12%) lone pairs. The pertinent orbital, the 155a (σ^*) lies at nearly the same energy as the σ^* of the *trans* complex, suggesting that the σ-interaction between the Pd $4d_{xy}$ and the ligand lone pairs has a comparable strength in the two complexes. A support to this suggestion comes from the Mulliken gross population analysis showing that the charge transfer from the ligands to the Pd $4d_{xy}$ is nearly the same in the two complexes (1.02 vs 1.00 electrons). At variance with the *trans* complex, the σ^* is not the LUMO, however. Now, the LUMO (154a) is an almost-pure π^*_{bipy} MO and lies 0.73 eV lower than the σ^*. The other lowest π^*_{bipy} MOs, the 156a and 157a, are located immediately above the σ^*.

TDDFT Calculations of the Electronic Absorption Spectra. To provide an assignment of the main spectral features of the two complexes, TDDFT calculations of the lowest excited states have been performed. Simulated electronic absorption spectra and a stick diagram of the energy

https://doi.org/10.1021/acs.inorgchem.1c01092
Inorg. Chem. XXXX, XXX, XXX−XXX

and oscillator strength of the lowest excited states are shown in Figure 6. The calculated excitation energies and oscillator strengths of the *trans*-$[(py)_2Pd(CBT)_2]$ and *cis*-$[(bipy)Pd(CBT)_2]$ complexes, in $CHCl_3$, are gathered in Tables 5 and 6, respectively. The tables also include the composition of the excited states, in terms of one-electron transitions.

When comparing the simulated and experimental spectra of the two complexes, it is apparent that the experimental spectral profiles are reproduced quite well theoretically, although the energy of the main features is slightly overestimated by the calculations. Considering first the *trans*-$[(py)_2Pd(CBT)_2]$ complex, the TDDFT results indicate that the most intense band appearing in the spectrum at 322 nm originates from the 1^1A_g $(S_0) \rightarrow 3^1A_u$ (S_3) excitation computed at 297 nm and with oscillator strength of 0.963. According to its composition, the 3^1A_u excited state originates from the $74a_u \rightarrow 80a_g$ $S_{lp} \rightarrow \sigma^*$ transition. The much weaker 1^1A_g $(S_0) \rightarrow 1^1A_u$ (S_1) excitation calculated at 353 nm and with the same $S_{lp} \rightarrow \sigma^*$ character contributes to the red tail of the 322 absorption. In the 270−237 nm energy range, we compute four excited states of appreciable intensity and with $S_{lp} \rightarrow \pi^*_{py}$ interligand character, the 4^1A_u, 7^1A_u, 8^1A_u, and 9^1A_u. Of these, the 4^1A_u, 7^1A_u and 8^1A_u are responsible for the shoulder at ∼253 nm, the most intense 9^1A_u accounts for the absorption rising to the blue of this shoulder.

Coming to the *cis*-$[(bipy)Pd(CBT)_2]$ complex, the best candidates for assignment of the very broad and weak absorption in the 330−550 nm region are the 2^1A, 3^1A, and 8^1A excited states that involve transitions out of S_{lp} and/or mixed S_{lp}/metal orbitals into the σ^*. The longest wavelength absorption at 450 nm, which is peculiar of the electronic spectrum of the *cis* complex, is accounted for by the $S_0 \rightarrow S_2$ $(1^1A \rightarrow 2^1A)$ excitation computed at 413 nm and with oscillator strength of 0.019. According to the composition of the 2^1A excited state in Table 6, this state originates from a transition out of a pure S_{lp} MO, the 153-HOMO, into the σ^*. In the *trans* complex, the excited state having the same character as the 2^1A is the 1^1A_u. This state has nearly the same oscillator strength as the 2^1A (0.018 vs 0.019) but is computed at a shorter wavelength (353 nm vs 413 nm) because the MO out of which the one-electron transition responsible for this state originates, the $75a_u$, is lower in energy than the corresponding MO of the *cis* complex, the 153a (−7.31 eV vs −6.88 eV).

The 3^1A and 8^1A excited states contributing to the broad and more intense features at shorter wavelength than the 450 nm absorption have a dominant d,d character and have no counterpart in the *trans* complex. In the 330−550 nm region, we also find excited states with extremely weak intensity (not shown in Table 6) involving transitions from the HOMO and HOMO−1 into the 154a π^*_{bipy} MO and hence with a clear interligand CT character.

The quite intense feature appearing in the spectrum of the *cis*-$[(bipy)Pd(CBT)_2]$ complex at 308 nm is assigned to the $S_0 \rightarrow S_{11}$ $(1^1A \rightarrow 11^1A)$ and $S_0 \rightarrow S_{12}$ $(1^1A \rightarrow 12^1A)$ excitations. The former transition has a clear intra ligand $\pi^*_{bipy} \rightarrow \pi^*_{bipy}$ character, the latter has a charge transfer (CT) character as it originates from a one-electron transition out of the 150a that is largely localized on the S_{lp} and Pd $4d_{xz}$ orbitals, into a π^*_{bipy} MO, the 154a. The quite intense $S_0 \rightarrow S_{13}$ $(1^1A \rightarrow 13^1A)$ excitation can be assigned to the low-energy tail of the asymmetric band peaking at 250 nm nicely accounted for by the $S_0 \rightarrow S_{17}$ $(1^1A \rightarrow 17^1A)$ excitation computed at 253 nm and with oscillator strength of 0.401. As inferred from the excited-state compositions in Table 6, the 17^1A state has a multitransition character and involves one-electron transitions out of metal or mixed metal/S_{lp} orbitals into the σ^* or π^*_{bipy} MOs. The rather intense $S_0 \rightarrow S_{16}$ $(1^1A \rightarrow 16^1A)$ and $S_0 \rightarrow S_{18}$ $(1^1A \rightarrow 18^1A)$ excitations computed at 255 and 252 nm, are likely to contribute to the intensity of the feature with a maximum at 250 nm.

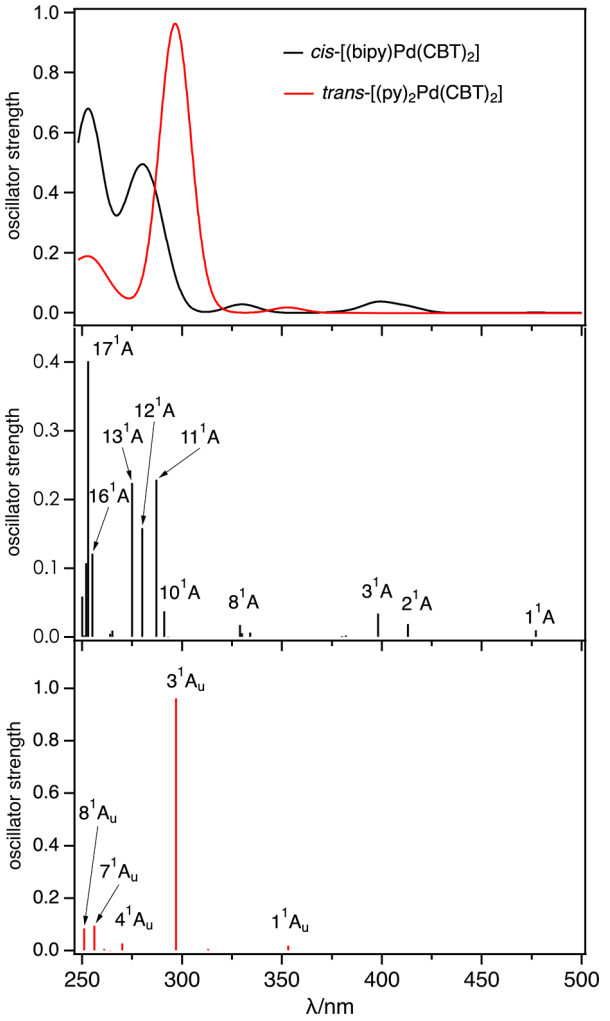

Figure 6. TDDFT/ZORA/CAMY-B3LYP/TZ2P simulated electronic absorption spectra (top) and stick diagram of the energy and oscillator strength (bottom) of the lowest excited states of *trans*-$[(py)_2Pd(CBT)_2]$ and *cis*-$[(bipy)Pd(CBT)_2]$ in $CHCl_3$.

In conclusion, the intense near-UV features appearing at 322 nm in the *trans* complex and at 308 nm in the *cis* complex have a quite different character, the former originating from a $S_{lp} \rightarrow \sigma^*$ transition, the latter from a $\pi_{bipy} \rightarrow \pi^*_{bipy}$ intraligand and a S_{lp}, $4d_{xz} \rightarrow \pi^*_{bipy}$ charge-transfer transition.

Moreover, the absorption appearing in the electronic spectrum of the *cis*-$[(bipy)Pd(CBT)_2]$ complex (and of the $[\{Pd(CBT)_2\}_4LM]\cdot xH_2O$ pentanuclear complexes) at ∼450 nm is clearly related to the *cis* arrangement of the CBT groups, because the $S_{lp} \rightarrow \sigma^*$ transition responsible for this absorption shifts to longer wavelength upon going from the *trans* to the *cis* CBT derivative, because of the upshift of the pertinent S_{lp} lone pair MO.

Mechanism of the *cis*-$[(bipy)Pd(CBT)_2]$ → *trans*-$[(py)_2Pd(CBT)_2]$ Conversion. In this section, we discuss the

https://doi.org/10.1021/acs.inorgchem.1c01092
Inorg. Chem. XXXX, XXX, XXX−XXX

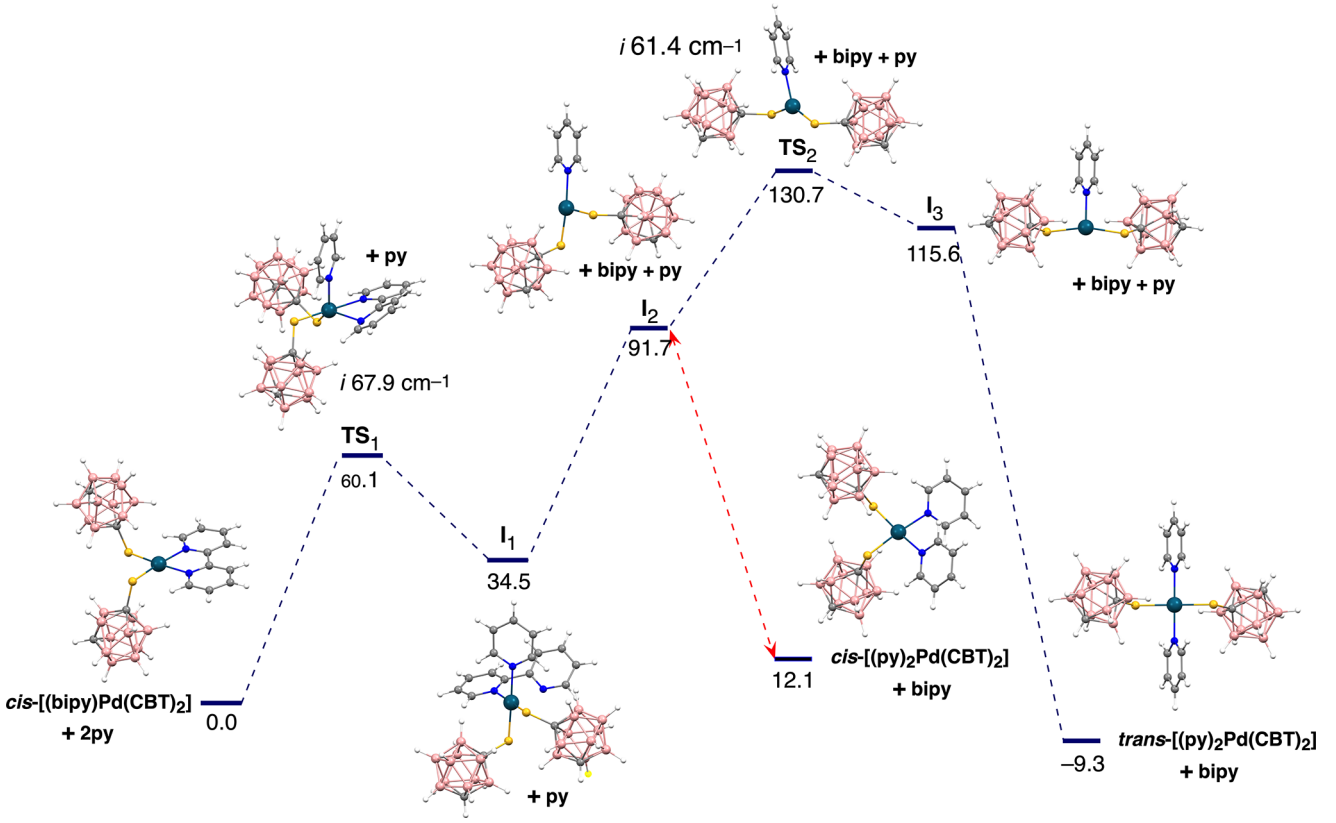

Figure 7. Potential energy profile for the reaction of *cis*-[(bipy)Pd(CBT)$_2$] with pyridine in $CHCl_3$. The molecular structures of the species involved in the reaction are also shown. The energies are in kJ/mol and include ZPE correction and solvation effects.

DFT results concerning the mechanism of the *cis*-[(bipy)Pd(CBT)$_2$] → *trans*-[(py)$_2$Pd(CBT)$_2$] conversion reaction. The potential energy profile for the reaction is shown in Figure 7, and the relevant energy data are summarized in Table 7.

Table 7. Energy Data for the *cis*-[(bipy)Pd(CBT)$_2$] → *trans*-[(py)$_2$Pd(CBT)$_2$] Conversion

energy term	value (kJ/mol)
ΔE_{TS_1}	60.1
ΔE_{I_1}	34.5
ΔE_{I_2}	57.8
ΔE_{P_1}	12.1
ΔE_{TS_2}	39.0
ΔE_{I_3}	23.9
ΔE_P	–9.3

[a] $\Delta E_{TS_1} = E(\mathbf{TS_1}) - E(\mathbf{R})$ ($\mathbf{R}$ = *cis*-[(bipy)Pd(CBT)$_2$] + 2py); $\Delta E_{I_1} = E(\mathbf{I_1}) - E(\mathbf{R})$; $\Delta E_{I_2} = E(\mathbf{I_2}) - E(\mathbf{I_1})$; $\Delta E_{P_1} = E(\mathbf{P_1}) - E(\mathbf{R})$ ($\mathbf{P_1}$ = *cis*-[(py)$_2$Pd(CBT) $_2$] + bipy); $\Delta E_{TS_2} = E(\mathbf{TS_2}) - E(\mathbf{I_2})$; $\Delta E_{I_3} = E(\mathbf{I_3}) - E(\mathbf{I_2})$; $\Delta E_P = E(\mathbf{P}) - E(\mathbf{R})$ ($\mathbf{P}$ = *trans*-[(py)$_2$Pd(CBT) $_2$] + bipy).

The key geometrical features of the species involved in the reaction are shown in Figures 8 and 10, as well as in Figures S3 and S4 in the Supporting Information.

The first step of the reaction was investigated through a relaxed PES scan in which the distance between Pd and the incoming pyridine N3 atom (see Figure 8) was chosen as the reaction coordinate.

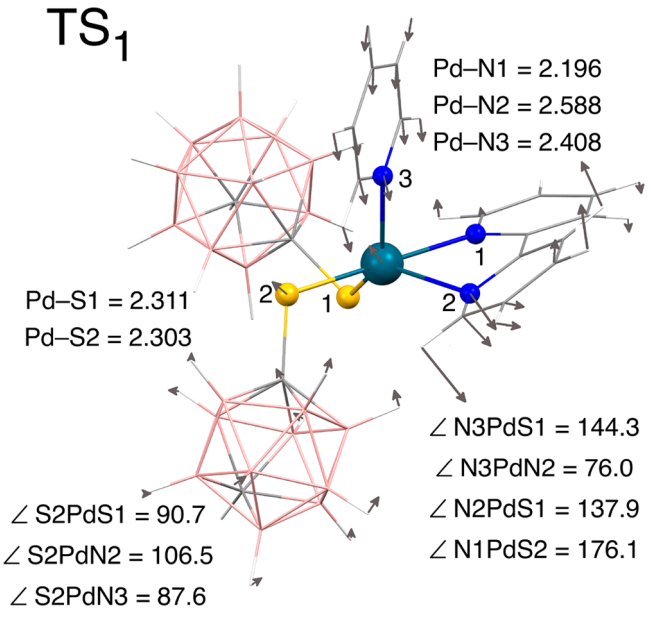

Figure 8. DFT/ZORA/CAMY-B3LYP/TZP optimized structure of $\mathbf{TS_1}$ with bond lengths in angstroms and angles in degrees. The associated normal mode is also shown.

The entering pyridine was placed at a position 3.000 Å above the *cis*-[(bipy)Pd(CBT)$_2$] molecular plane and the Pd–N3 distance was reduced in steps of 0.100 Å up to 2.200 Å. The corresponding minimum energy path (MEP) was easily followed, allowing the determination of a good guess for the full optimization of the transition state ($\mathbf{TS_1}$, detailed in Figure

https://doi.org/10.1021/acs.inorgchem.1c01092
Inorg. Chem. XXXX, XXX, XXX–XXX

8). According to this study, the first step proceeds through a *distorted* trigonal bipyramidal transition state, as found in virtually all substitution reactions at square planar reaction centers.[27] In $\mathbf{TS_1}$ the entering pyridine occupies an equatorial position in the trigonal bipyramid and is bent toward the N2 atom of the leaving arm of bipy (<N3PdN2 = 76°). Such a bending, which is driven by the necessity to relieve the steric hindrance between the pyridine π-system and the B−H bonds of the carborane cage opposite to N2, *sums up* to the labilizing effect of the trans CBT ligand facilitating the substitution reaction. As a matter of fact, the geometrical parameters in Figure 8 show that, in $\mathbf{TS_1}$, the incoming pyridine ligand is closer to Pd than the leaving arm of bipy (d_{Pd-N3} = 2.408 Å and d_{Pd-N2} = 2.588 Å), which means that we are dealing with a rather early transition state, in keeping with the relatively low energy barrier of 60.1 kJ/mol (Table 7). We note, in passing, that the preliminary B3LYP/def2-SV(P) calculations provided a similar description of the first pyridine attack. Actually, the gas-phase $\mathbf{TS_1}$ energy computed at the B3LYP/def2-SV(P) level was 47.5 kJ/mol, compared to the 44.7 kJ/mol value computed in the gas phase at the ZORA/CAMY-B3LYP/TZP level.

Because of the lengthening of the Pd−N2 bond, the two pyridines of bipy are no longer coplanar in the transition state, the dihedral angle between them amounting to 22.2°. This angle further increases (35.4°) upon relaxation of $\mathbf{TS_1}$ toward the intermediate *cis*-[(k^1-bipy)(py)Pd(CBT)$_2$] species, $\mathbf{I_1}$, where the Pd−N2 bond is virtually broken (d_{Pd-N2} = 2.917 Å) and the pertinent pyridine moiety of bipy is replaced by the entering pyridine, so restoring the square planar coordination of the central metal (Figure S3 in the Supporting Information).

To get more insight into the intimate mechanism underlying the formation of $\mathbf{TS_1}$, we have performed an energy decomposition analysis of the interaction energy, ΔE_{int}, between the *cis*-[(bipy)Pd(CBT)$_2$] complex and the entering pyridine ligand in the reactant complex (a complex in which the metal center of the complex is weakly bound to the pyridine nitrogen lone pair) en route to $\mathbf{TS_1}$, and at $\mathbf{TS_1}$ (Pd−N3 = 2.408 Å). According to the energy terms gathered in Table 8, the stabilizing ΔV_{elstat} term becomes more and more negative as the $\mathbf{TS_1}$ is approached.

The destabilizing ΔE_{Pauli} term also increases as the $\mathbf{TS_1}$ is approached, less rapidly in the proximity of $\mathbf{TS_1}$, however, to the result that the $\Delta E^0(\Delta E_{Pauli} + \Delta V_{elstat})$ term that is increasingly destabilizing in the range 2.808−2.458 Å drops at the transition state. As for the attractive ΔE_{oi} term, this is increasingly stabilizing, not enough however to overcome the destabilizing ΔE^0 term, except that at the transition state, where the ΔE_{int} ($\Delta E^0 + \Delta E_{oi}$) term is −40.6 kJ/mol. Electronic structure analysis of the interacting fragments en route to $\mathbf{TS_1}$ reveals that the orbital interaction term, ΔE_{oi}, largely accounts for the charge transfer out of the pyridine lone pair (the 21a-HOMO) into the Pd 5p$_y$ and 5p$_x$ orbitals, and, in the close proximity of the transition state, also into the Pd 4d$_{xy}$ that at this stage becomes suitable for interaction. According to the Mulliken gross population analysis of the fragment orbitals the charge transfer from the pyridine 21a MO into the metal orbitals amounts to only 0.02 electrons at 2.808 Å but becomes 0.10 electrons at the transition state. Note that, initially, the pyridine lone pair interacts with the *occupied* MOs of the *cis*-[(bipy)Pd(CBT)$_2$] fragment with large amplitude on the Pd 4d$_{z^2}$ and/or 4d$_\pi$ orbitals (see Figure 9a for an example).

Table 8. Energy Decomposition Analysis of the Interaction Energy ΔE_{int} (kJ/mol) Between the *cis*-[(bipy)Pd(CBT)$_2$] Complex and the Entering Pyridine Ligand at $\mathbf{TS_1}$ (Pd−N3 = 2.408 Å) and En Route to $\mathbf{TS_1}$

	Interaction Energy, ΔE_{int} (kJ/mol)				
	Pd−N3 = 2.808 Å	Pd−N3 = 2.608 Å	Pd−N3 = 2.508 Å	Pd−N3 = 2.458 Å	Pd−N3 = 2.408 Å
ΔE_{Pauli}	93.1	149.5	193.9	220.7	222.6
ΔV_{elstat}	−69.6	−109.1	−141.6	−161.9	−189.9
$\Delta E^0(\Delta E_{Pauli} + \Delta V_{elstat})$	23.5	40.4	52.3	58.8	32.6
ΔE_{oi}	−25.8	−38.1	−47.4	−53.0	−73.2
ΔE_{int} ($\Delta E^0 + \Delta E_{oi}$)	−2.3	2.4	4.8	5.8	−40.6

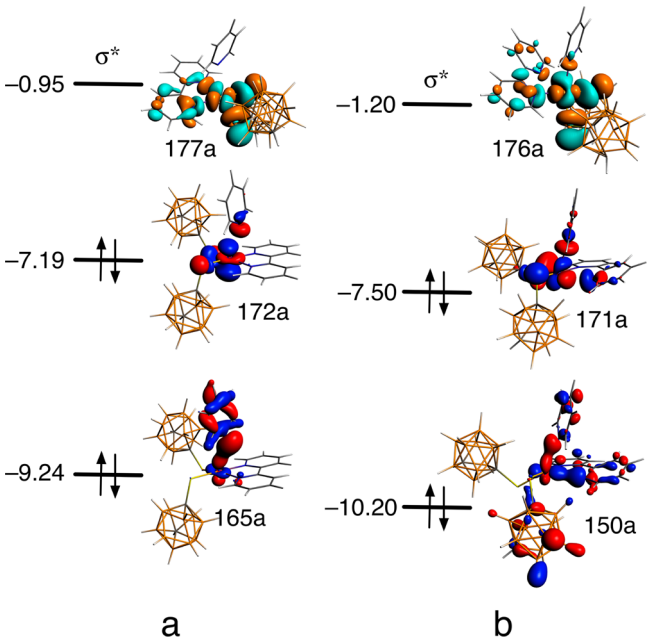

Figure 9. Schematic level diagrams of (a) selected MOs of the reactant complexen route to $\mathbf{TS_1}$ (Pd−Npy = 2.808 Å) and (b) at $\mathbf{TS_1}$. The contour values are ±0.04 e/au^3.

Although these interactions represent mostly Pauli repulsion, they enable the just-mentioned charge transfer, thanks to the admixture of the Pd-based occupied MOs with the Pd 5p$_y$ and 5p$_x$ orbitals.

In the close proximity of $\mathbf{TS_1}$, the pyridine lone pair mainly interacts with the empty Pd 4d$_{xy}$, leading to a more effective pyridine to metal charge transfer and, hence, to a more stabilizing ΔE_{oi} term. The interaction of the pyridine 21a with the Pd 4d$_{xy}$ at the transition state is apparent from the plot of the 176a-σ^* in Figure 9b.

At this point one may wonder whether the first step of the conversion reaction could occur through a dissociative path leading to the dangling k^1-bipy ligand, followed by a fast coordination of the entering pyridine. To verify this, we have computed at B3LYP/def2-SV(P) level the energy barrier of the dissociative step and found that it amounts to 106.1 kJ/mol, a value that reasonably rules out any competition with the associative mechanism discussed above. Therefore, the alternative dissociative mechanism was no further investigated.

The second step of the reaction consists in the *cis*-[(k^1-bipy)(py)Pd(CBT)$_2$] → *trans*-[(py)$_2$Pd(CBT)$_2$] isomerization

https://doi.org/10.1021/acs.inorgchem.1c01092
Inorg. Chem. XXXX, XXX, XXX−XXX

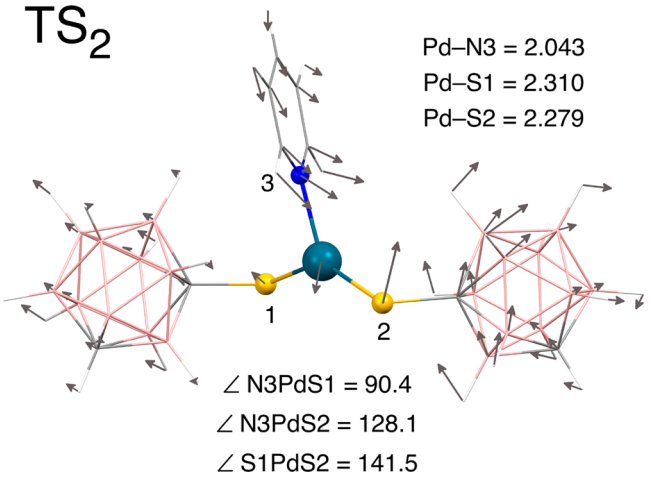

Figure 10. DFT/ZORA/CAMY-B3LYP/TZP optimized structure of $\mathbf{TS_2}$ with bond lengths in angstroms and angles in degrees. The associated normal mode is also shown.

reaction. Once formed, the $\mathbf{I_1}$ intermediate releases the dangling kN^1-bipy ligand forming the three-coordinate T-shaped *cis*-[(py)Pd(CBT)$_2$] species, $\mathbf{I_2}$. This dissociative process is endothermic by only 57.2 kJ/mol, which is consistent with the Pd–N1 bond being relatively weak in $\mathbf{I_1}$ (Pd–N1 = 2.189 Å) (see Figure S3 in the Supporting Information) and was described by the calculations as a barrierless step. Involvement of a three-coordinate T-shaped intermediate species in the *cis*-to-*trans* and *trans*-to-*cis* isomerization reactions of square planar d^8 complexes has already been reported.[28]

The direct attack of the second pyridine on $\mathbf{I_1}$ through an associative mechanism was also explored. However, the performed relaxed scans and direct searches of an associative transition state were unsuccessful in the gas phase and in $CHCl_3$ solution (COSMO), both at B3LYP/def2-SV(P) and ZORA/CAMY-B3LYP/TZP level of theory. A direct attack of the solvent ($CHCl_3$) on $\mathbf{I_1}$ was also explored through relaxed PES scans. Again, no associative pathways were found.

Once obtained from $\mathbf{I_1}$, the $\mathbf{I_2}$ intermediate may convert to the *trans*-counterpart $\mathbf{I_3}$ through $\mathbf{TS_2}$ and/or react with the excess of pyridine to afford the *cis*-[(py)$_2$Pd(CBT)$_2$] complex. However, this complex is rather unstable thermodynamically and, albeit formed, is likely to rapidly release one pyridine to reform the $\mathbf{I_2}$ species and, hence, convert to the *trans*-counterpart $\mathbf{I_3}$ through $\mathbf{TS_2}$. On the other hand, there was no evidence of formation of the *cis*-[(py)$_2$Pd(CBT)$_2$] complex after reaction of *cis*-[(bipy)Pd(CBT)$_2$] with pyridine and any attempt to synthesize the *cis*-[(py)$_2$Pd(CBT)$_2$] complex was unsuccessful. According to the ΔE_{TS_2} value in Table 7, the conversion of the *cis*-[(py)Pd(CBT)$_2$] species into the trans-counterpart $\mathbf{I_3}$ occurs through an energy barrier of only 39.0 kJ/mol. Any involvement of the solvent ($CHCl_3$) in the $\mathbf{I_2} \rightarrow \mathbf{I_3}$ isomerization reaction was ruled out by the calculations. $CHCl_3$ resulted indeed unable to occupy the fourth coordination site of the metal in $\mathbf{I_2}$.

Upon reaction with pyridine $\mathbf{I_3}$ evolves toward the final product, the *trans*-[(py)$_2$Pd(CBT)$_2$] complex. This process is highly exothermic (−125.2 kJ/mol) and drives the conversion of $\mathbf{I_1}$ into the final product that is more stable than its isomer *cis*-[(py)$_2$Pd(CBT)$_2$] and the starting complex, the *cis*-[(bipy)Pd(CBT)$_2$], by 21.4 and 9.3 kJ/mol, respectively. From the potential energy profile in Figure 7 and the energy data in Table 7, we may conclude that the second step of the *cis*-[(bipy)Pd(CBT)$_2$] → *trans*-[(py)$_2$Pd(CBT)$_2$] reaction is the rate-determining step. The energy barrier, which comprises the $\mathbf{I_1}$ dissociation energy and the $\mathbf{I_2}$ isomerization energy, indeed amounts to 96.8 kJ/mol.

CONCLUSIONS

The *trans*-[(py)$_2$Pd(CBT)$_2$] species previously obtained upon reaction with pyridine of the (∼py)$_2$Pd(CBT)$_2$ groups appended to the periphery of the [{Pd(CBT)$_2$}$_4$LZn]·xH$_2$O complex[4] has now been directly prepared by reaction of *trans*-[(py)$_2$PdCl$_2$] with CBTH. A parallel and appropriately adapted synthetic procedure has also been used to synthesize the bis CBT analogue *cis*-[(bipy)Pd(CBT)$_2$] taken as a model of the (∼py)$_2$Pd(CBT)$_2$ groups. Both complexes have been thoroughly characterized by IR and UV–vis spectroscopy, as well as via single-crystal X-ray studies and DFT/TDDFT calculations of the ground and excited states. The UV–vis spectra of the two complexes in various nonaqueous solvents exhibit intense absorptions in the region below 400 nm, but only the cis complex shows a very broad and weak absorption to the red of the near-UV intense band, in the 330–550 nm region, with detectable features at 356 and 450 nm in $CHCl_3$. The position and intensity of the 450 nm feature are consistent with those exhibited by the absorption appearing in the 400–500 nm region of the spectra of the [{Pd(CBT)$_2$}$_4$LZn]·xH$_2$O pentanuclear complex and previously associated with the presence of the peripheral (∼py)$_2$Pd(CBT)$_2$ groups. To understand why in the [(py)$_2$Pd(CBT)$_2$] complex formed upon reaction of the pentanuclear species with pyridine the CBT units assume a trans instead of the cis arrangement they show in the pentanuclear complex, the *cis*-[(bipy)Pd(CBT)$_2$] complex was reacted with pyridine in $CHCl_3$ solution and in neat pyridine. In both solvents, the reaction quantitatively afforded the *trans*-[(py)$_2$Pd(CBT)$_2$] complex, just as observed for the pentanuclear complex.

DFT calculations of the ground-state molecular structure well reproduce the observed elongation of the Pd–N bonds and concomitant shortening of the Pd–S bonds upon going from the *trans*-[(py)$_2$Pd(CBT)$_2$] to the *cis*-[(bipy)Pd(CBT)$_2$] complex, a behavior that is most likely related to a significant trans influence of the thiolate ligands on the Pd–N bonds.

Analysis of the ground-state electronic structure of the *trans*-[(py)$_2$Pd(CBT)$_2$] and *cis*-[(bipy)Pd(CBT)$_2$] complexes reveals that replacement of the pyridines by bipy and the *trans* to *cis* arrangement change of the CBT ligands have appreciable effects on the energy and composition of the frontier MOs. In particular, upon going from the *trans* to the *cis* complex, the highest occupied S_{lp}-based MOs uptshift and the LUMO is no longer the σ^*, which in both complexes lies at nearly the same energy, but the lowest π^*_{bipy} MO.

TDDFT calculations of the lowest excited states nicely reproduce the experimental spectral profiles, although the energy of the main features is slightly overestimated. From the composition of the excited states, in terms of one-electron transitions, it emerges that the intense near-UV feature appearing at 322 nm in the *trans* complex and at 308 nm in the *cis* complex have a quite different character, the former originating from a $S_{lp} \rightarrow \sigma^*$ transition, the latter from a combination of $\pi^*_{bipy} \rightarrow \pi^*_{bipy}$ and S_{lp}, $4d_{xz} \rightarrow \pi^*_{bipy}$ transitions. Moreover, it is found that the absorption appearing in the electronic spectrum of the *cis*-[(bipy)Pd(CBT)$_2$] complex

https://doi.org/10.1021/acs.inorgchem.1c01092
Inorg. Chem. XXXX, XXX, XXX–XXX

(and of the $[\{Pd(CBT)_2\}_4LM]\cdot xH_2O$ pentanuclear complexes) at ~450 nm originates from a $S_{lp} \rightarrow \sigma^*$ transition and is related to the cis arrangement of the CBT groups.

The theoretical study of the mechanism of the *cis*-$[(bipy)Pd(CBT)_2] \rightarrow$ *trans*-$[(py)_2Pd(CBT)_2]$ conversion reaction shows that the process occurs in two steps. In the first step, one arm of the bipy ligand is replaced by pyridine through an associative mechanism that involves a trigonal bipyramidal transition state and has a quite low energy barrier of 60.1 kJ/mol. The second step is the rate-determining step of the reaction, the energy barrier amounting to 95.3 kJ/mol. This step involves the dissociation of the bipy ligand with formation of the three-coordinate T-shaped *cis*-$[(py)Pd(CBT)_2]$ species (ΔE = 57.2 kJ/mol) and subsequent isomerization of this species into the trans counterpart (ΔE_{TS_2} = 39.0 kJ/mol) that eventually affords the *trans*-$[(py)_2Pd(CBT)_2]$ product after reaction with pyridine.

■ ASSOCIATED CONTENT

Supporting Information

The Supporting Information is available free of charge at https://pubs.acs.org/doi/10.1021/acs.inorgchem.1c01092.

IR spectra of the investigated complexes (Figure S1). Crystal structure of the *cis*-$[(bipy)Pd(CBT)_2]$ complex (Figure S2). DFT/ZORA/CAMY-B3LYP/TZP optimized structures of the $\mathbf{I_1}$ and $\mathbf{I_2}$ species involved in the *cis*-$[(bipy)Pd(CBT)_2] \rightarrow$ *trans*-$[(py)_2Pd(CBT)_2]$ conversion reaction (Figure S3). DFT/ZORA/CAMY-B3LYP/TZP optimized structures of the *cis*-$[(py)_2Pd(CBT)_2]$ and $\mathbf{I_3}$ species involved in the *cis*-$[(bipy)Pd(CBT)_2] \rightarrow$ *trans*-$[(py)_2Pd(CBT)_2]$ conversion reaction (Figure S4). Cartesian coordinates of the *cis*-$[(bipy)Pd(CBT)_2]$ and *trans*-$[(py)_2Pd(CBT)_2]$ complexes optimized in the gas phase at the DFT/ZORA/CAMY-B3LYP/TZ2P level of theory. Cartesian coordinates of the *cis*-$[(bipy)Pd(CBT)_2]$ and *trans*-$[(py)_2Pd(CBT)_2]$ complexes optimized in $CHCl_3$ at DFT/ZORA/CAMY-B3LYP/COSMO/TZ2P level of theory. Cartesian coordinates of the species involved in the *cis*-$[(bipy)Pd(CBT)_2] \rightarrow$ *trans*-$[(py)_2Pd(CBT)_2]$ conversion upon reaction with pyridine optimized in the gas-phase at DFT/ZORA/CAMY-B3LYP/TZP level of theory (PDF)

Accession Codes

CCDC 2076203 contains the supplementary crystallographic data for this paper. These data can be obtained free of charge via www.ccdc.cam.ac.uk/data_request/cif, or by emailing data_request@ccdc.cam.ac.uk, or by contacting The Cambridge Crystallographic Data Centre, 12 Union Road, Cambridge CB2 1EZ, UK; fax: +44 1223 336033.

■ AUTHOR INFORMATION

Corresponding Authors

Maria Pia Donzello − *Dipartimento di Chimica, Università di Roma Sapienza, I-00185 Roma, Italy*; orcid.org/0000-0001-9084-0369; Email: mariapia.donzello@uniroma1.it

Corrado Rizzoli − *Dipartimento di Scienze Chimiche, della Vita e della Sostenibilità Ambientale, Università di Parma, I-43124 Parma, Italy*; orcid.org/0000-0002-4841-6123; Email: corrado.rizzoli@unipr.it

Mario Amati − *Dipartimento di Scienze, Università della Basilicata, I-85100 Potenza, Italy*; Email: mario.amati@unibas.it

Authors

Noemi Bellucci − *Dipartimento di Chimica, Università di Roma Sapienza, I-00185 Roma, Italy*

Elisa Viola − *Dipartimento di Chimica, Università di Roma Sapienza, I-00185 Roma, Italy*

Claudio Ercolani − *Dipartimento di Chimica, Università di Roma Sapienza, I-00185 Roma, Italy*

Giampaolo Ricciardi − *Università della Basilicata, Scuola di Scienze Agrarie, Forestali, Alimentari e Ambientali (SAFE), I-85100 Potenza, Italy*; orcid.org/0000-0002-6034-8813

Angela Rosa − *Dipartimento di Scienze, Università della Basilicata, I-85100 Potenza, Italy*; orcid.org/0000-0003-4592-244X

Complete contact information is available at: https://pubs.acs.org/10.1021/acs.inorgchem.1c01092

Notes

The authors declare no competing financial interest.

■ ACKNOWLEDGMENTS

Financial support by the University of Rome Sapienza (Progetto di Ricerca−Anno 2019 RP11916B889D3C2D) is gratefully acknowledged. This research work was partially supported by the Università degli Studi della Basilicata, Italy.

■ REFERENCES

(1) Nedunchezhian, K.; Aswath, N.; Thiruppathy, M.; Thirugnanamurthy, S. Boron Neutron Capture Therapy—A Literature Review. *J. Clin. Diagn. Res.* **2016**, *10*, ZEO1−ZEO4.

(2) Issa, F.; Kassiou, M.; Rendina, L. M. Boron in Drug Discovery: Carboranes as Unique Pharmacophores in Biologically Active Compounds. *Chem. Rev.* **2011**, *111*, 5701−5722.

(3) Hu, K.; Yang, Z.; Zhang, L.; Xie, L.; Wang, L.; Xu, H.; Josephson, L.; Liang, S. H.; Zhang, M.-R. Boron agents for neutron capture therapy. *Coord. Chem. Rev.* **2020**, *405*, 213139.

(4) Viola, E.; Donzello, M. P.; Testani, S.; Luccisano, G.; Astolfi, M. L.; Rizzoli, C.; Cong, L.; Mannina, L.; Ercolani, C.; Kadish, K. M. Tetra-2,3-pyrazinoporphyrazines with Peripherally Appended Pyridine Rings. 19. Pentanuclear Octa(2-pyridyl)-tetrapyrazinoporphyrazines Carrying Externally Carboranthiolate Groups: Physicochemical Properties and Potentialities as Anticancer Drugs. *Inorg. Chem.* **2019**, *58*, 1120−1133.

(5) Bellucci, N.; Donzello, M. P.; Viola, E.; Ercolani, C. Homo/Heteropentanuclear Porphyrazine Mg^{II}, Zn^{II}, Pd^{II} Macrocycles with Externally Pending $PdCl_2$ and $Pd(CBT)_2$ Units. Synthesis, Physicochemical Characterization, and Photoactivity Studies. Manuscript submitted for publication.

(6) (a) Spokoyny, A. M.; Machan, C. W.; Clingerman, D. J.; Rosen, M. S.; Wiester, M. J.; Kennedy, R. D.; Stern, C. L.; Sarjeant, A. A.; Mirkin, C. A. A coordination chemistry dichotomy for icosahedral carborane-based ligands. *Nat. Chem.* **2011**, *3*, 590−596. (b) Pal, M. K.; Jain, V. K.; Wadawale, A. P.; Glazun, S. A.; Starikova, Z. A.; Bregadze, V. I. Synthesis and spectroscopy of cis-configured mononuclear palladium(II) and platinum(II) complexes of chalcogeno o-carboranes and structures of $[Pt(SCb^oPh)_2(dppm)]$, $[Pt(SeCb^oPh)_2(dppm)]$, $[Pt(SCb^oS)(PMe_2Ph)_2]$ and $[Pt(SCb^oS)(PMePh_2)_2]$. *J. Organomet. Chem.* **2012**, *696*, 4257−4263. (c) Kennedy, R. D.; Stern, C. L.; Mirkin, C. A. Zwitterionic Weak-Link Approach Complexes Based on Anionic Icosahedral Monocarbaboranes. *Inorg. Chem.* **2013**, *52*, 14064−14077.

(7) Kharasch, M. S.; Seyler, R. C.; Mayo, F. R. Coördination Compounds of Palladous Chloride1. *J. Am. Chem. Soc.* **1938**, *60*, 882−884.
(8) (a) Viossat, B.; Dung, N.-H.; Robert, F. Structure du trans-dichlorobis(pyridine)palladium(II). *Acta Crystallogr., Sect. C: Cryst. Struct. Commun.* **1993**, *49*, 84−85. (b) Liao, C.-Y.; Lee, H. M. trans-Dichlorodipyridinepalladium(II). *Acta Crystallogr., Sect. E: Struct. Rep. Online* **2006**, *62*, m680−m681. (c) Lee, H. M.; Liao, C.-Y. A new monoclinic polymorph of trans-dichloridodipyridinepalladium(II). *Acta Crystallogr., Sect. E: Struct. Rep. Online* **2008**, *64*, No. m1447.
(9) Maekawa, M.; Munakata, M.; Kitagawa, S.; Nakamura, M. Crystal Structure of (2,2′-Bipyridine)dichloropalladiun(II). *Anal. Sci.* **1991**, *7*, 521−522.
(10) *APEX2, S. a. S.*; Bruker Axs, Inc.: Madison, WI, USA, 2008.
(11) Sheldrick, G. SHELXT - Integrated space-group and crystal-structure determination. *Acta Crystallogr., Sect. A: Found. Adv.* **2015**, *71*, 3−8.
(12) Sheldrick, G. Crystal structure refinement with SHELXL. *Acta Crystallogr., Sect. C: Struct. Chem.* **2015**, *71*, 3−8.
(13) (a) ADF2019, SCM *Theoretical Chemistry*; Vrije Universiteit, Amsterdam, The Netherlands, http://www.scm.com. (b) Baerends, E. J.; Ellis, D. E.; Ros, P. Self-consistent molecular Hartree—Fock—Slater calculations I. The computational procedure. *Chem. Phys.* **1973**, *2*, 41−51. (c) te Velde, G.; Bickelhaupt, F. M.; Baerends, E. J.; Fonseca Guerra, C.; van Gisbergen, S. J. A.; Snijders, J. G.; Ziegler, T. Chemistry with ADF. *J. Comput. Chem.* **2001**, *22*, 931−967.
(14) Seth, M.; Ziegler, T. Range-Separated Exchange Functionals with Slater-Type Functions. *J. Chem. Theory Comput.* **2012**, *8*, 901−907.
(15) (a) van Lenthe, E.; Baerends, E. J.; Snijders, J. G. Relativistic regular two-component Hamiltonians. *J. Chem. Phys.* **1993**, *99*, 4597−4610. (b) van Lenthe, E.; Baerends, E. J.; Snijders, J. G. Relativistic total energy using regular approximations. *J. Chem. Phys.* **1994**, *101*, 9783−9792. (c) van Lenthe, E.; Ehlers, A.; Baerends, E. J. Geometry optimizations in the zero order regular approximation for relativistic effects. *J. Chem. Phys.* **1999**, *110*, 8943−8953.
(16) Van Lenthe, E.; Baerends, E. J. Optimized Slater-type basis sets for the elements 1−118. *J. Comput. Chem.* **2003**, *24*, 1142−1156.
(17) (a) Klamt, A.; Schüürmann, G. COSMO: a new approach to dielectric screening in solvents with explicit expressions for the screening energy and its gradient. *J. Chem. Soc., Perkin Trans. 2* **1993**, 799−805. (b) Klamt, A. Conductor-like Screening Model for Real Solvents: A New Approach to the Quantitative Calculation of Solvation Phenomena. *J. Phys. Chem.* **1995**, *99*, 2224−2235. (c) Pye, C. C.; Ziegler, T. An implementation of the conductor-like screening model of solvation within the Amsterdam density functional package. *Theor. Chem. Acc.* **1999**, *101*, 396−408.
(18) (a) Becke, A. D. DFT thermochemistry III. The role of exact exchange. *J. Chem. Phys.* **1993**, *98*, 5648−5652. (b) Lee, C.; Yang, W.; Parr, R. G. Development of the Colle-Salvetti correlation-energy formula into a functional of the electron density. *Phys. Rev. B: Condens. Matter Mater. Phys.* **1988**, *37*, 785−789.
(19) Weigend, F.; Ahlrichs, R. Balanced basis sets of split valence, triple zeta valence and quadruple zeta valence quality for H to Rn: Design and assessment of accuracy. *Phys. Chem. Chem. Phys.* **2005**, *7*, 3297−3305.
(20) Andrae, D.; Häußermann, U.; Dolg, M.; Stoll, H.; Preuß, H. Energy-adjustedab initio pseudopotentials for the second and third row transition elements. *Theor. Chim. Acta* **1990**, *77*, 123−141.
(21) *Gaussian 09*, Revision D.01, M. J., Frisch, Trucks, G. W.; Schlegel, H. B.; Scuseria, G. E.; Robb, M. A.; Cheeseman, J. R.; Scalmani, G.; Barone, V.; Mennucci, B.; Petersson, G. A.; Nakatsuji, H.; Caricato, M.; Li, X.; Hratchian, H. P.; Izmaylov, A. F.; Bloino, J.; Zheng, G.; Sonnenberg, J. L.; Hada, M.; Ehara, M.; Toyota, K.; Fukuda, R.; Hasegawa, J.; Ishida, M.; Nakajima, T.; Honda, Y.; Kitao, O.; Nakai, H.; Vreven, T.; Montgomery, J. A., Jr.; Peralta, J. E.; Ogliaro, F.; Bearpark, M.; Heyd, J. J.; Brothers, E.; Kudin, K. N.; Staroverov, V. N.; Keith, T.; Kobayashi, R.; Normand, J.; Raghavachari, K.; Rendell, A.; Burant, J. C.; Iyengar, S. S.; Tomasi, J.; Cossi, M.; Rega, N.; Millam, J. M.; Klene, M.; Knox, J. E.; Cross, J. B.; Bakken, V.; Adamo, C.; Jaramillo, J.; Gomperts, R.; Stratmann, R. E.; Yazyev, O.; Austin, A. J.; Cammi, R.; Pomelli, C.; Ochterski, J. W.; Martin, R. L.; Morokuma, K.; Zakrzewski, V. G.; Voth, G. A.; Salvador, P.; Dannenberg, J. J.; Dapprich, S.; Daniels, A. D.; Farkas, O.; Foresman, J. B.; Ortiz, J. V.; Cioslowski, J.; Fox, D. J. *Gaussian 09*, Revision D.01, Gaussian, Inc., Wallingford CT, 2013.
(22) Morokuma, K. Molecular Orbital Studies of Hydrogen Bonds. III. C = OMMMH−O Hydrogen Bond in $H_2COCCCH_2O$ and $H_2COCCC2H_2O$. *J. Chem. Phys.* **1971**, *55*, 1236−1244.
(23) Ziegler, T.; Rauk, A. On the calculation of bonding energies by the Hartree Fock Slater method. *Theor. Chim. Acta* **1977**, *46*, 1−10.
(24) Bickelaupt, F. M.; Baerends, E. J. In *Reviews in Computational Chemistry*, Vol. *15*; Lipkowitz, K. B., Boyd, D. R., Eds.; Wiley: New York, 2000; pp 1−86.
(25) (a) Fujimoto, H.; Osamura, Y.; Minato, T. Orbital interaction and chemical bonds. Exchange repulsion and rehybridization in chemical reactions. *J. Am. Chem. Soc.* **1978**, *100*, 2954−2959. (b) Kitaura, K.; Morokuma, K. A new energy decomposition scheme for molecular interactions within the Hartree-Fock approximation. *Int. J. Quantum Chem.* **1976**, *10*, 325−340. (c) van den Hoek, P. J.; Kleyn, A. W.; Baerends, E. J. What is the origin of the repulsive wall in atom-atom potentials. *Comments At. Mol. Phys.* **1989**, *23*, 93−110.
(26) Leites, L. A. Vibrational spectroscopy of carboranes and parent boranes and its capabilities in carborane chemistry. *Chem. Rev.* **1992**, *92*, 279−323.
(27) (a) Basolo, F.Bridging groups in electron transfer reactionsA-merican Chemical Society In *Mechanisms of Inorganic Reactions*; Advances in Chemistry Series, Vol. *49*; American Chemical Society: Washington, DC, 1965; pp 81−106. (b) Purcell, K. F.; Kotz, J. C.*Inorganic Chemistry*; Saunders, 1977.
(28) (a) Ozawa, F.; Ito, T.; Nakamura, Y.; Yamamoto, A. Mechanisms of Thermal Decomposition of trans- and cis-Dialkylbis-(tertiary phosphine)palladium(II). Reductive Elimination and trans to cis Isomerization. *Bull. Chem. Soc. Jpn.* **1981**, *54*, 1868−1880. (b) Minniti, D. Uncatalyzed Cis-Trans Isomerization of Bis-(pentafluorophenyl)bis(tetrahydrothiophene)palladium(II) Complexes in Chloroform: Evidence for a Dissociative Mechanism. *Inorg. Chem.* **1994**, *33*, 2631−2634. (c) Hildebrand, A.; Sárosi, I.; Lönnecke, P.; Silaghi-Dumitrescu, L.; Sárosi, M. B.; Silaghi-Dumitrescu, I.; Hey-Hawkins, E. Heteropolytopic Arsanylarylthiolato Ligands: Cis−Trans Isomerism of Nickel(II), Palladium(II), and Platinum(II) Complexes of 1-AsPh2−2-SHC_6H_4. *Inorg. Chem.* **2012**, *51*, 7125−7133. (d) Guido, E.; D'Amico, G.; Russo, N.; Sicilia, E.; Rizzato, S.; Albinati, A.; Romeo, A.; Plutino, M. R.; Romeo, R. Mechanistic Insight into Protonolysis and Cis−Trans Isomerization of Benzylplatinum(II) Complexes Assisted by Weak Ligand-to-Metal Interactions. A Combined Kinetic and DFT Study. *Inorg. Chem.* **2011**, *50*, 2224−2239.

https://doi.org/10.1021/acs.inorgchem.1c01092
Inorg. Chem. XXXX, XXX, XXX−XXX